Effects of plasticity-induced martensitic transformation and grain refinement on the evolution of microstructure and mechanical properties of a metastable high entropy alloy

Shubhrodev Bhowmik[a], Jianzhong Zhang[b], Sven C. Vogel[b], Saurabh S. Nene[c,d], Rajiv S. Mishra[d], Brandon A. McWilliams[e], Marko Knezevic[a,*]

[a]Department of Mechanical Engineering, University of New Hampshire, Durham, NH, 03824, USA

[b]Materials Science and Technology Division, Los Alamos National Laboratory, Los Alamos, NM, 87545, USA.

[c]Department of Metallurgical and Materials Engineering, Indian Institute of Technology Jodhpur, Karwar, Jodhpur, Rajasthan 342037.

[d]Department of Materials Science and Engineering, University of North Texas, Denton, TX, 76207, USA.

[e]Weapons and Materials Research Directorate, DEVCOM Army Research Laboratory, Aberdeen Proving Ground, MD, 21005, USA.

Abstract

This paper describes the main results from an experimental investigation into tailoring the phase content and grain structure for high strength of a microstructurally flexible high entropy alloy (HEA), $Fe_{42}Mn_{28}Co_{10}Cr_{15}Si_5$ (in at%), using rolling, friction stir processing (FSP), and compression. Optical microscopy, neutron diffraction, and electron backscatter diffraction were employed to characterize microstructure and texture evolution. The material upon rolling was found to have triplex structure consisting of metastable gamma austenite (γ), stable sigma (σ), and stable epsilon martensite (ε) phases. The adaptive phase stability exhibited by the selected HEA of very low stacking fault energy with strain, strain rate, and temperature was used along with grain refinement to enhance the strength. To this end, the complex structure was refined by FSP at 350 revolutions per minute (RPM) tool rotation rate, while increasing the fraction of γ and decreasing the σ and ε content. The strength was further enhanced by FSP at 150 RPM by further refinement of the grain structure and increasing the fraction of ε phase. The peak ultimate tensile strength of ~1850 MPa was achieved by double pass FSP (350 RPM followed by 150 RPM), the sequence which even more refined the microstructure and increased the fraction of σ phase. While the content of diffusion created σ phase remains constant during subsequent compression, the fraction

* Corresponding author at: University of New Hampshire, Department of Mechanical Engineering, 33 Academic Way, Kingsbury Hall, W119, Durham, New Hampshire 03824, United States.
E-*mail address*: marko.knezevic@unh.edu (M. Knezevic).

of ε increases due to the diffusionless strain induced $\gamma \rightarrow \varepsilon$ phase transformation. The transformation facilitates plastic strain accommodation and rapid strain hardening, which has been attributed to the increase in highly dislocated ε phase fraction and transformation induced dynamic Hall-Petch-type barrier effect. Interestingly, a great deal of hardening ability was exhibited by the HEA even at very high strength. Roles of texture, grain size, and phase content on the transformation during compression have been rationalized and discussed in this paper.

Keywords: High entropy alloys; Friction stir processing; Phase transformations; Grain structure; Texture

1 Introduction

In an effort to maximize the strengthening effect of solid solution while avoiding brittle intermetallic phases, a special class of sophisticated materials termed high entropy alloys (HEAs) are being developed [1, 2]. These materials have shown the potential to improve the contrasting material properties of strength and ductility. An equiatomic HEA like $Fe_{20}Mn_{20}Ni_{20}Co_{20}Cr_{20}$ is an example HEA exhibiting outstanding strength, ductility, and fracture toughness at both cryogenic and room temperatures [1]. Beyond the equiatomic HEAs, other variants of the Fe-Mn-Ni-Co-Cr HEA system like $Fe_{40}Mn_{27}Ni_{26}Co_5Cr_2$ (at. %) or different types of non-equiatomic HEAs are being explored, e.g., $Al_{33.4}Co_{22.2}Cr_{11.1}Fe_{22.2}Ni_{11.1}$ (at. %) [3-7]. The primary advantage of HEAs pertains to the tunable microstructure and deformation characteristics by modifying the composition and processing. For example, dual phase HEAs (DP-HEAs) of Fe-Mn-Co-Cr were developed, e.g. $Fe_{50}Mn_{30}Co_{10}Cr_{10}$ (all in at. %) to contain austenite (γ) of face-centered cubic (FCC) structure, which is a metastable phase undergoing the strain-induced phase transformation to highly dislocated epsilon martensite phase (ε) with hexagonal close-packed (HCP) structure [6, 8]. The mechanism is referred to as the transformation induced plasticity (TRIP), and in addition to dislocation slip, is a predominant deformation mode in these alloys. As a result, these HEAs offer an opportunity to design volume fraction and thermodynamic stability of γ-austenite and ε-martensite to increase both ductility and strength [3, 4, 6]. In addition to TRIP and slip, twinning induced plasticity (TWIP) can also operate in HEAs offering an additional degree of freedom for plastic deformation and hardening [9]. Accordingly, stacking fault energy (SFE) of a given alloy must be low enough to decrease the critical stress for twin formation or to allow the separation between partial dislocations forming shear bands of ε-martensite phase [10]. The TWIP is promoted in the range $\sim 20 < SFE < 40$ mJ/m^2, while the TRIP is promoted for SFE$<\sim$15 mJ/m^2 [11-15].

Studies into the effect of increasing Cr at the expense of Fe and Mn alloying elements on γ phase in DP-HEA have been carried out in [14, 16]. It is found that adding extra Cr increases the driving force of $\gamma \rightarrow \varepsilon$ phase transformation. For example, in the case of $Fe_{47}Mn_{28}Co_{10}Cr_{15}$, the extra 5% of Cr decreases the γ phase fraction at room temperature with a very small change to the onset temperature (T_0) of transformation. Additionally, the effect of adding non transition elements such as C, Al, and Si on Fe-Mn alloys was explored using thermodynamic simulations [16]. Following these initial works, the effect of Si in $Fe_{47}Mn_{28}Co_{10}Cr_{15}$ alloy was investigated with

thermodynamic calculations. The work found that adding 5% of Si increases the T_0 to a threshold value of 425 ^{0}C as well as the metastability of γ phase [17]. In summary, Si has the advantage over other elements like Ni and Al in terms of providing increased γ phase metastability and higher T_0 value (i.e. stable ($\gamma + \varepsilon$) phase field until a higher temperature). As a result, a new composition was developed with an alloy chemistry of $Fe_{42}Mn_{28}Cr_{15}Co_{10}Si_5$ (all in at. %) referred to as DP-5Si-HEA. The alloy in its as-cast condition exhibits about 100 MPa increase in YS relative to the as-cast $Fe_{50}Mn_{30}Co_{10}Cr_{10}$ DP-HEA, while ~600 MPa increase in YS after M-pass compared to the as-cast DP-HEA counterpart [3, 4, 17]. Recently, a HEA ($Fe_{40}Mn_{20}Co_{20}Cr_{15}Si_5$ (all in at. %), also known as CS-HEA because of the increased amount of Co and added Si relative to the reference DP-HEA, $Fe_{50}Mn_{30}Co_{10}Cr_{10}$, from [4], was developed to take the advantages of both TRIP and TWIP [6, 12]. In this alloy, increased Co in addition to Si stabilize and promote ε-martensite by lowering the SFE [13-15]. The large fraction of ε phase promotes strain accommodation by twinning and pyramidal slip. Interestingly a decrease in $\frac{c}{a}$ ratio of ε-martensite from 1.619 in the initial microstructure to 1.588 at fracture upon tension was reported for this alloy [18].

The enhanced metastability of γ phase can also enhance the temperature, strain, and strain rate sensitive phase evolution in HEAs during thermomechanical processing [13-15]. To this end, deformation processing of such material via rolling or forging can substantially change their microstructure [12]. The microstructural changes can be even more dramatic by processing of the material using high temperature severe plastic deformation techniques such as equal channel angular pressing (ECAP), high pressure torsion (HPT), and friction stir processing (FSP) [19-21]. Significant enhancements in strength and ductility over as-cast $Fe_{40}Mn_{30}Co_{10}Cr_{15}Si_5$ (in at%) HEA was obtained via FSP processing because of intense grain refinement and larger fraction of high angle grain boundaries [9, 21, 22]. In contract, intense grain refinement via fragmentation of grains due to dislocation storage in ECAP and HPT results in large fractions of low angle grain boundaries [23, 24].

The as-cast DP-5Si-HEA provides the ($\gamma + \varepsilon$) mixture with more dominance of γ phase [17]. The multi-pass friction stir processing of the alloy (M-pass, 3 overlapping passes with 650 rotations per minute (RPM) in the first pass down to 350 RPM in the second pass and to 250 RPM in the third pass) refined the grain size from 100 μm to 1.3 μm as well as increased the ε phase fraction [17]. The FSP increased the yield strength (YS) to 950 MPa with an ultimate tensile

strength (UTS) of 1.15 GPa relative to the cast 400 MPa YS. The alloy after FSP had a ductility of 7%. These improvements in mechanical properties after FSP have been associated to the increase in metastability of γ phase, which promotes $\gamma \rightarrow \varepsilon$ phase transformation and subsequent twinning in the ε phase.

To complement the above research involving the as-cast DP-5Si-HEA and FSP, this paper is concerned with studying the changes in the microstructure and associated mechanical properties upon hot rolling of the $Fe_{42}Mn_{28}Co_{10}Cr_{15}Si_5$ (in at%) composition (DP-5Si-HEA). The evolution of microstructure and texture was measured by optical microscopy, neutron diffraction (NeD), and electron back scatter diffraction (EBSD). The material upon rolling was found to have triplex structure consisting of metastable γ-austenite, stable σ-phase, and stable ε-martensite phases. The rolled HEA was further processed by FSP using a range of process parameters to potentially take advantage of metastability of γ phase while tuning its strength and deformation characteristics. Simple compression tests were performed on as-rolled and FSP materials to study strength and the evolution of phases: volume fraction, size, and texture. These microstructural features were measured and quantified. Based on the data, roles of texture, grain size, and phase content in the initial microstructure on the transformation rate in the presence of three phases and associated mechanical properties during compression have been rationalized and discussed. Moreover, the changes of the c/a ratio was observed and underlying implications on the shifts in active deformation mechanisms and ductility have been discussed.

2 Experimental procedures

2.1 Material processing

The rolled plate of $Fe_{42}Mn_{28}Co_{10}Cr_{15}Si_5$ (in at%) HEA was received from Sophisticated Alloys, Inc. After casting a 50.8 mm thick ingot, the ingot went through a homogenization heat treatment at 1100^0C for 2 hrs. Right upon the heat treatment, the ingot was rolled into a plate of 8.9 mm thickness in multiple passes.

The rolled plate was processed by FSP following the procedures presented in [25, 26]. A W-RE processing tool was used with a shoulder diameter of 12 mm and the root diameter of 7.5 mm.

The shoulder also contained a tapered pin of 6 mm in diameter and 3.5 mm in length. Since the length of the tool was 3.5 mm, the depth of FSP beads would be ~3.7 mm. Based on the bead dimensions, the diameter and height of the compression cylinders were determined.

Three different FSP beads were created with varying tool rotational rates in the plate. The 1st FSP bead was made with a tool rotational rate of 350 RPM (100 mm long bead), the 2nd bead was made with 150 RPM tool rotational rate (80 mm long bead), and the 3rd bead was made with two overlapping passes of 350 RPM followed by 150 RPM tool rotational rate (120 mm long bead). The traverse speed was 50.8 mm/min for all. The FSP was performed along the transverse direction (TD) of the rolled plate. Samples for compression were machined from the four regions and classified into four categories: as-rolled, 350 RPM FSP, 150 RPM FSP, and 350 RPM followed by 150 RPM FSP denoted as "A", "B", "C" and "D", respectively.

2.2 Mechanical testing

Cylinders for compression testing were machined by wire electrical discharge machining (EDM) in two plate directions: (1) the in-plane (IP) along the TD direction, the direction which is also parallel to the FSP direction (FSPD) and (2) the through thickness (TT) direction or the normal direction (ND) of the plate. The purpose of making samples in two different directions is to evaluate any plastic anisotropy in compression. 3 mm and 4 mm diameter TT and IP cylinders were made for the four categories of samples. Height of B, C, and D category cylinders was 3 mm in both TT and IP directions. Only 3 mm diameter cylinders were used for the IP direction testing because of the bead height. Height of the A category cylinders was 4.8 mm.

An Instron servo hydraulic testing machine model #1350 was used for compression testing. The tests were performed at room temperature and under a constant strain rate of $10^{-3}/\mathrm{s}$. The machine is equipped with a load cell of 100 kN capacity, hardened steel compression fixtures, and DAX software. Oil was used as a lubricant to minimize the effects of friction between compression dies and the sample. By placing a ball between the upper force arm and upper die, uniaxial state of the test was better ensured. Compliance of the testing setup was measured and subtracted from the raw compression data to correct load vs. displacement data before calculating the true stress-true strain curves. The tests were performed either to fracture or interrupted at given strain levels.

Samples upon the interrupted tests were used to measure microstructural evolution. The tests to fracture were repeated at least three times to ensure accuracy of the data.

2.3 Microstructural characterization

2.3.1 Microscopy

To characterize the microstructure both optical microscopy and EBSD in a scanning electron microscope (SEM) were performed. The optical imaging was performed using Olympus OLS5000 capable of performing scans by both laser and visible light. All the images reported here were taken by laser. The EBSD was performed in a Tescan Lyra (Ga) field emission type of SEM equipped with Pegasus system (Octane Plus SDD detector and Hikari High Speed Camera). Scans were performed in the depth mode with a spot size of 50 - 320 nm and 19.4 -20 beam intensity (BI) at a voltage of 10-15 kV. The working distance was kept at ~8.9 mm. To obtain statistically significant data multiple scans were taken for each category of the materials. For samples with bigger grains, larger areas were scanned, while for fine grains samples, the scan size was small. All the scans contained about 500,000 - 1,000,000 points with step size 0.2-0.6 μm for scans with bigger grains and 0.03-0.05 μm for scans with fine grains. Post processing of collected data was performed using the analysis software package OIM 8.

The samples from all categories were prepared by grinding with SiC papers from 180 to 1200 grit. After grinding, the samples were polished by 3, and 1 μm glycol based polycrystalline diamond solution with red lubricant. As for the final step, 0.05 μm master-prep alumina was used. The optical microscopy imaging was performed after etching with Kalling's-2 reagent for 5-10 s. The etching solution is comprised of 5g of $CuCl_2$, 100 ml of HCl, 100 ml ethanol (C_2H_5OH).

Energy dispersive spectroscopy (EDS) was also carried out at 15 kV voltage and 9 mm working distance to observe the elemental composition of phases present in the microstructure.

2.3.2 Neutron diffraction

NeD was performed in Los Alamos Neutron Science Center (LANSCE) at Los Alamos National Laboratory [27]. The facility is equipped with a time-of-flight (TOF) high-pressure-preferred orientation (HIPPO) neutron diffractometer with pulsed neutron source. The diffractometer contains five HIPPO detector rings at the nominal diffraction angles of 144°, 120°,

90°, 60°, and 40°. The cylinders were oriented such that the loading direction (LD) is perpendicular to the incoming neutron beam. Three different sample orientations (0°, 67.5°, and 90°), with each having count time about an hour and average proton current 100 μA, provided 132 histograms from all five detector rings. For phase analysis, the diffraction data was binned with 5 rings and three rotations were integrated to create single histograms for each detector rings or banks. These made the phase analysis largely free from the texture influence for each bank and easier to identify the minority phases. The orientation distribution function (ODF) was calculated from 132 histograms, which were binned with 45 panels. This way of analysis provided the necessary statistical accuracy for texture analysis since all 132 histograms are being fitted to complete the whole Debye ring. A software package called Maud was used to analyze the experimental histograms [28].

3 Results

3.1 Mechanical testing

True stress – true strain curves recorded during compression testing of the materials in the four conditions are shown in Fig. 1. As is evident, the as-rolled A material category has the lowest strength. The as-rolled material is approximately isotropic and able to accumulate more compressive strain in IP than in TT. The strength of the material increases with FSP. Since FSP was performed at different tool rates, the true stress – true strain curves and underlying microstructures are different. Decreasing the tool speed from 350 RPM to 150 RPM and performing the double pass increase the strength of the material. The D category material tested along the IP direction exhibits the highest strength reaching 1850 MPa UTS. The increase in strength from C to D material did not result in substantial loss of strain to fracture. This is attributed to similar accommodation of plastic strain in the samples, and in particular, to the extent of the TRIP effect. The FSP materials show some anisotropy with the higher strength in the IP than in the TT direction. The directional dependence of the compressive strength is attributed to the microstructure morphology created by FSP and the difference in the rate of TRIP with texture. To rationalize the strength behavior of the materials, microscopy and NeD characterizations were performed, and these results are presented in the next section.

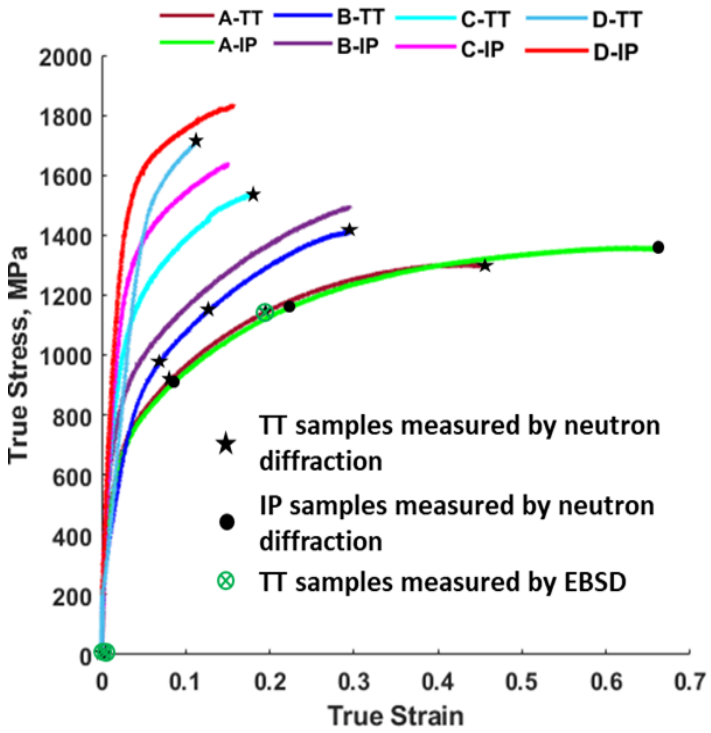

Figure 1: True stress - true strain curves for the four categories of the samples compressed to fracture in both in-plane (IP) and through thickness (TT) directions. Several compression tests are interrupted before fracture at the strain levels indicated by the symbols for the NeD and EBSD characterization.

3.2 Microstructural characterization

3.2.1 EBSD

The inverse pole figure maps (IPF) and phase maps are shown in Fig. 2 for the four material categories before compression testing. Three phases are identified with green, red, and yellow colors, which corresponds to γ-austenite, ε-martensite and σ-phase. While the γ and ε phases are solid solution of all the 5 elements (Fe, Mn, Co, Cr, Si), the σ phase is an intermetallic of slightly increased Fe and Cr content with tetragonal crystal structure. The higher percentage of Cr (>15 wt%) increases the probability of σ-phase formation in the range between 600^0C and 1000^0C at favorable cooling rates in stainless steels [29, 30]. However, the use of Si along with higher Cr than typical for the Fe-Mn-Co-Cr systems (10 at%) can increase the propensity of σ-phase precipitation [31, 32].

The average grain size of γ phase was estimated in every scan and provided in Table 1. The grain size was estimated keeping the grain misorientation angle at 15°. The annealing twins observed in A-TT were not considered during the grain size calculation. As is evident, the as-rolled A category samples have the largest average grain size of ~20 μm. Because the as-rolled grain structure is refined with FSP, the average grain size in the B category samples is ~4 μm. The FSP conditions at 350 RPM provide a heat input into the material facilitating some grain growth and increase in the amount of γ phase content. The fraction of ε and σ phase slightly decreased in B samples relative to A samples. As a consequence of FSP at 150 RPM, the C category samples have average grain size of ~2 μm. Grain refinement as well as an increase in the ε phase volume fraction is achieved with the FSP at 150 RPM relative to the A samples. The D category samples showed both the major grain size refinement and a major increase in the σ phase volume fraction relative to the A category material. The D category samples show similar γ phase fractions to C category but the finest average grain size (~1 μm) because of the double pass FSP. The IPF maps of the FSP materials show some elongation of grains along the FSPD governing some anisotropy.

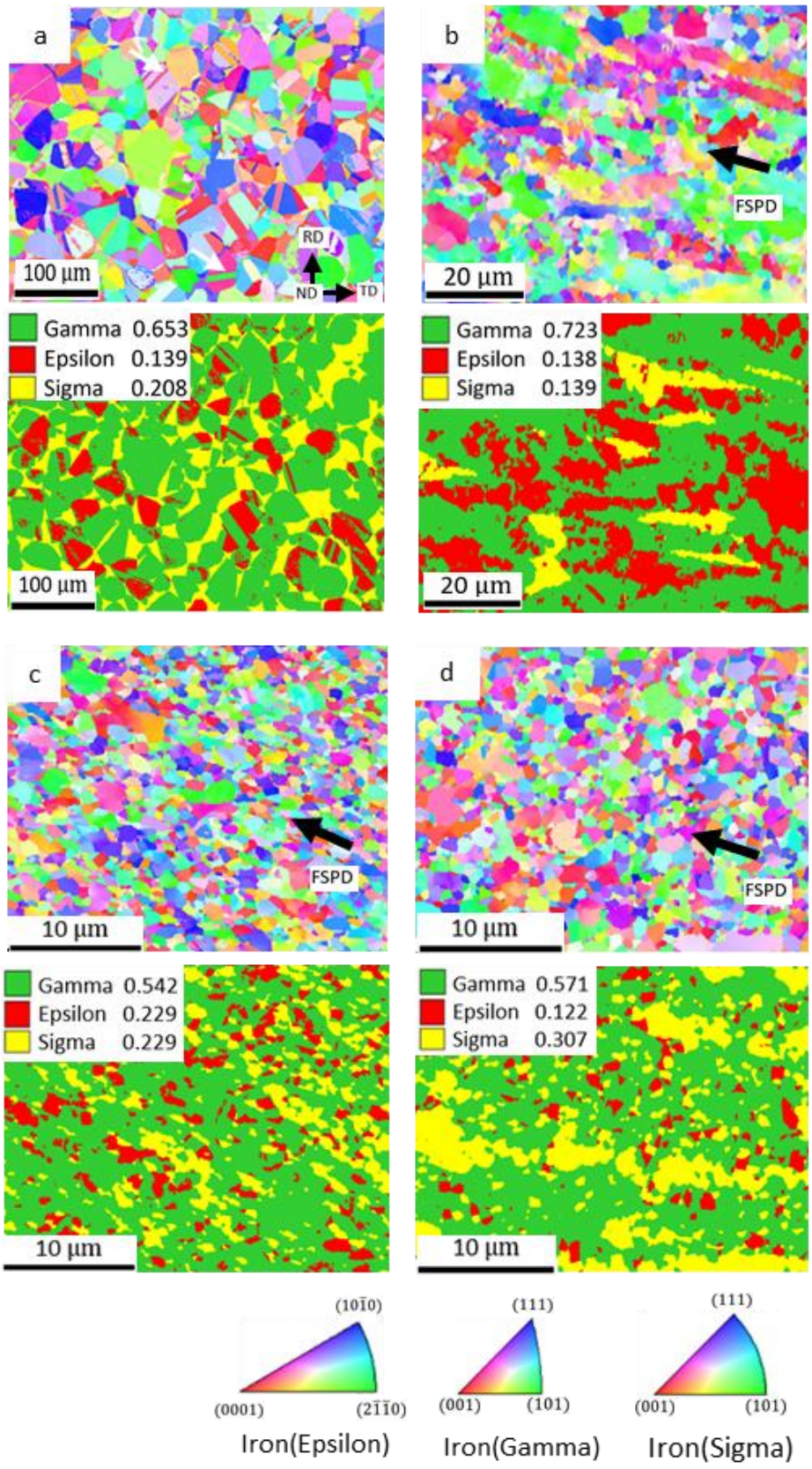
a
100 µm
RD
ND
TD
b
FSPD
20 µm
Gamma 0.653
Epsilon 0.139
Sigma 0.208
100 µm
Gamma 0.723
Epsilon 0.138
Sigma 0.139
20 µm
c
FSPD
10 µm
d
FSPD
10 µm
Gamma 0.542
Epsilon 0.229
Sigma 0.229
10 µm
Gamma 0.571
Epsilon 0.122
Sigma 0.307
10 µm
(10$\bar{1}$0)
(0001)
(2$\bar{1}\bar{1}$0)
Iron(Epsilon)
(111)
(001)
(101)
Iron(Gamma)
(111)
(001)
(101)
Iron(Sigma)

Figure 2: Inverse pole figure and phase maps acquired by EBSD for samples: (a) A-TT-initial (as rolled), (b) B-TT-initial (FSP at a tool speed of 350 rpm), (c) C-TT-initial (FSP at a tool speed of 150 rpm), and (d) D-TT-initial (double pass - FSP with two consecutive runs at tool speeds of 350 RPM and 150 RPM, respectively). Perpendicular to the maps is the sample TT direction. The colors in the IPF maps represent the orientation of ND/TT sample axis with respect to the crystal lattice frame according to the coloring in the standard IPF triangles. Phase fraction values are averages of at least two scans. Annealing twins are present in the A category samples and indicated with dark orange arrows.

Table 1: Average grain size in γ phase per sample category.

Category	FCC (μm)
A-TT-initial	20
B-TT-initial	4
C-TT-initial	2
D-TT-initial	1

3.2.2 Neutron diffraction analysis

The integrated histograms for 144^0 detector banks are shown in Fig. 3 for A-IP sample category for initial ($\epsilon = 0$), $\epsilon = 0.098$, $\epsilon = 0.216$ and fractured ($\epsilon = 0.669$) samples. Although there are four main categories of samples, histograms from only A-IP are shown to present the phase identification procedure. Such data for the other samples look similar. The Bragg reflections for the present phases are identified in the figure. It is evident that the intensity of γ phase decreases with increasing the amount of compressive strain, while the intensity of the ε phase increases. A procedure for extracting phase fractions from neutron diffraction in Maud was described in detail in [33]. Similar procedure was used here to analyze the phase fractions for the HEA material, as briefly described below. The integrated experimental histograms were fit by calculating the

contribution of individual phases present in the samples along with the contribution from the background.

Since the height of cylindrical samples was about 3-4 mm, the diffraction peaks from α and γ phases from screws made of stainless steel were observed. These screws were used to mount the sample onto the holder. During neutron diffraction Cd foil shields the sample holder in order to stop originating peaks from the holder. The slit (2 mm) used to focus the neutron beam onto the sample was also made of Cd [34]. The Cd peaks were observed to the backscatter (144^0, 120^0) banks emerging from the Cd slit. Additionally, the neutron spallation inside the metal tube during the production of neutron beam changes the wavelength of part of the beam and shows up as a hump in the histogram of 144^0 detector bank. After isolating the peaks from the background, the histograms were fitted with the phases present in the HEA samples to get the phase fractions.

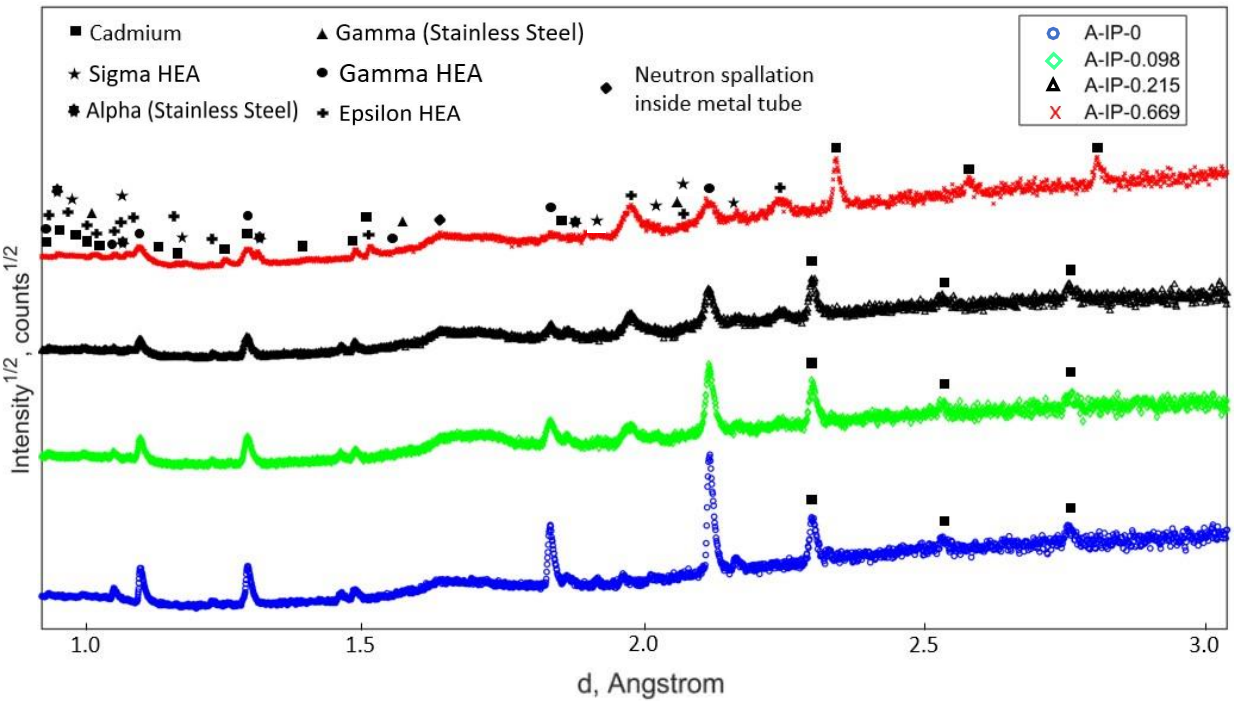

Figure 3: Phases in the neutron diffraction histograms for initial ($\epsilon = 0$), $\epsilon = 0.098$, $\epsilon = 0.216$ and fractured ($\epsilon = 0.669$) samples from A-IP category for 144 banks. The data from 2 mm slit is presented. The y-axis represents the square-root of the intensity of peaks in the square root of counts of photons, while the x-axis denotes the interplanar spacing (d-spacing). Since sigma phase has tetragonal crystal structure and has a lot of peaks, only selected ones were identified here. Some additional peaks are also identified such as cadmium, neutron spallation inside metal tube, and alpha and gamma phases from stainless steel. Cadmium was used to shield the sample holder

and as the slit during measurement and the peaks are only observed to the back scatter (144^0, 120^0) banks. The stainless steel (alpha and gamma phases) peaks originated from the screws, used to mount the small cylinders to a holder.

As mentioned in the previous sections, three phases of the HEA samples were extracted from the diffraction peaks. The Rietveld refinement was in the core of the procedure. The refinement was performed by refining the relevant crystallographic and scaling parameters of all the phases in order to increase the quality of least square fit between calculated and experimental diffraction histograms. At first, a fourth order polynomial was selected to fit each histograms background. After getting the background intensity of the calculated histogram close to the experimental one, the background was not refined in the further stages to avoid Cholesky negative diagonal per sample. The diffractometer constants (DIFC) were continuously refined in all steps through refining the basic parameters. In doing so, the lattice parameters of the three phases were also identified and has been discussed later. The micro-strain, which contributes to the peak broadening, was initially set to 6×10^{-4} με assuming a little effect on peak broadening. As refining heavily correlated variables such as crystallite size and micro-strain together can cause convergence issues, the crystallite size was kept fixed at ~1000 nm (meaning no peak broadening due to crystallite size in NeD). Since the atomic displacement parameters, B_{iso}, for the ε phase was not available in the literature, a weighted average of the B_{iso} of all five constituent elements (based on the at% of each element present in the material) was taken to get $B_{iso} = 0.43$. The B_{iso} of constituent elements were taken from the literature [35] and the intermetallic σ phase B_{iso} was kept at 0.8. The B_{iso} values were not refined during refinement process. After achieving convergence, the micro-strain was slightly refined. Since the crystallite size was kept fixed, the increase in the micro-strain values during the fitting is an indication of peak broadening and underlying increase in the dislocation density [36]. The atomic partial occupancies were set by literature values for all three phases and were not refined [37-39]. The parameters were refined in series to allow for convergence through the least-square fitting process.

Results of the phase analysis are presented in Fig. 4. The most evident change in the plots is the transformation of γ phase to ε as a consequence of the strain induced transformation process. The trends are approximately linear. In contrast to γ and ε, the σ phase fraction is unchanged under the compressive strain. The measurement for A-IP samples were performed with a 2 mm slit and

without a slit. The purpose of using a slit was to focus the neuron beam just on the sample and increase the accuracy. We can notice that the phase fractions obtained from 2 mm slit and without slit diffraction data are nearly identical verifying the accuracy of the measurements. The 2 mm slit neutron diffraction data was used to get the trend in phase transformation. Table 2 includes the linear trend fit parameters.

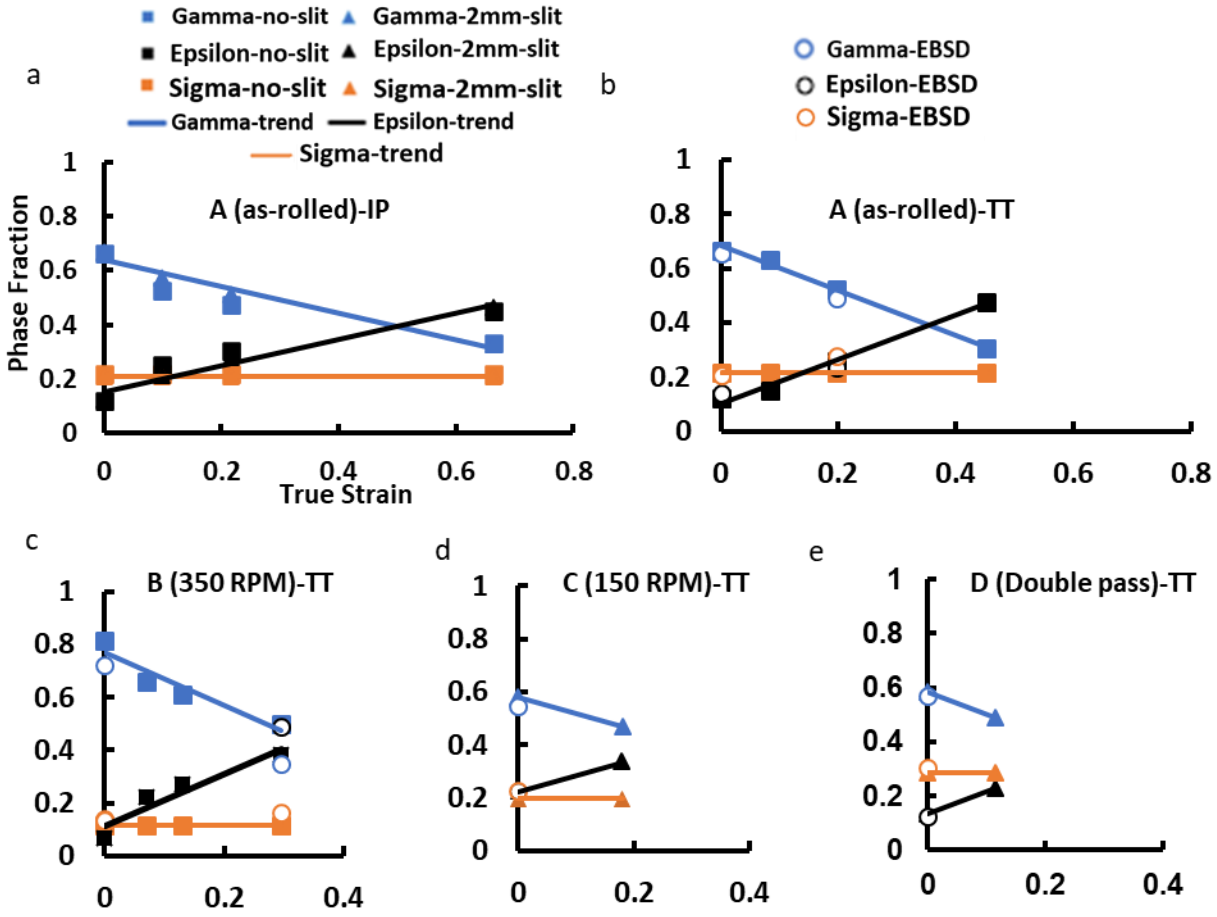

Figure 4: Evolution of phase fractions with plastic strain in compression for: (a) A-IP, (b) A-TT, (c) B-TT, (d) C-TT and (e) D-TT samples.

Table 2: Summary of the linear trend parameters for the evolution of phase fractions with plastic strain during compression measured by NeD: $P(\epsilon) = C_0 + C_1 \epsilon$; P = phase fraction and ϵ = true strain.

Category	Phase	C_0	C_1	R^2
A-TT	Gamma	0.682	-0.818	0.99
	Epsilon	0.100	0.818	0.99
	Sigma	0.218	0	---
A-IP	Gamma	0.639	-0.489	0.97
	Epsilon	0.151	0.485	0.97
	Sigma	0.210	0	---
B-TT	Gamma	0.768	-0.989	0.92
	Epsilon	0.113	0.989	0.90
	Sigma	0.118	0	---
C-TT	Gamma	0.579	-0.615	1.00
	Epsilon	0.223	0.615	1.00
	Sigma	0.197	0	---
D-TT	Gamma	0.583	-0.840	1.00
	Epsilon	0.132	0.840	1.00
	Sigma	0.285	0	---

During TOF neutron diffraction analysis, the sample has to be placed within ~0.1 m of the diffractometer center to achieve a precision of 10^{-4} to the lattice parameter. Otherwise, the diffractometer constant ($1/L\sin\theta$, where L is the total flight path) will be changed which could provide different lattice parameters [40, 41]. Since the cylinders were very small, it was difficult to achieve the exact alignment while mounting on the holder. Hence, the lattice parameters in

neutron diffraction are accurate to about two decimal points. From the phase fraction analyses of many samples, the average lattice parameters are inferred along with the standard deviation values: $a_{gamma} = 3.62374 \pm 0.02700$ Å, $a_{sigma} = 8.87510 \pm 0.07997$ Å and $c_{sigma} = 4.64307 \pm 0.04558$ Å with a ratio of 0.52315. These values agree well with the literature [37, 39]. Unlike the lattice parameters of γ and σ, we observe changes in the lattice parameters of ε-martensite. Such changes can occur due to the changes in chemical ordering or phase separations. The $\frac{c}{a}$ ratio changes are shown in Fig. 5. Interestingly, we observe that the ratio decreases but then increases during compression of the A and B samples.

Pole figures showing crystallographic texture evolution for γ and ε are presented in Fig. 6. The Rietveld refinement of all the 132 histograms from NeD data was used to reconstruct an ODF per sample for every phase. The analysis was performed using E-WMIV texture algorithm following the process described in [27, 34]. The initial texture in γ of A material category is a typical rolling texture of FCC metals. As expected, the pole figures for γ phase exhibit strengthening of $\{110\}$ fiber along the loading direction with compressive strain. For ε phase, the texture strengthens along the RD direction is primarily a consequence of phase transformation and some slip. There is no signature of deformation twinning in the texture of ε phase. The σ phase texture was also calculated but is not shown since it is very weak and approximately random. Texture appears relatively weak in all phases in all samples meaning that it likely has secondary effects on anisotropy in the material properties.

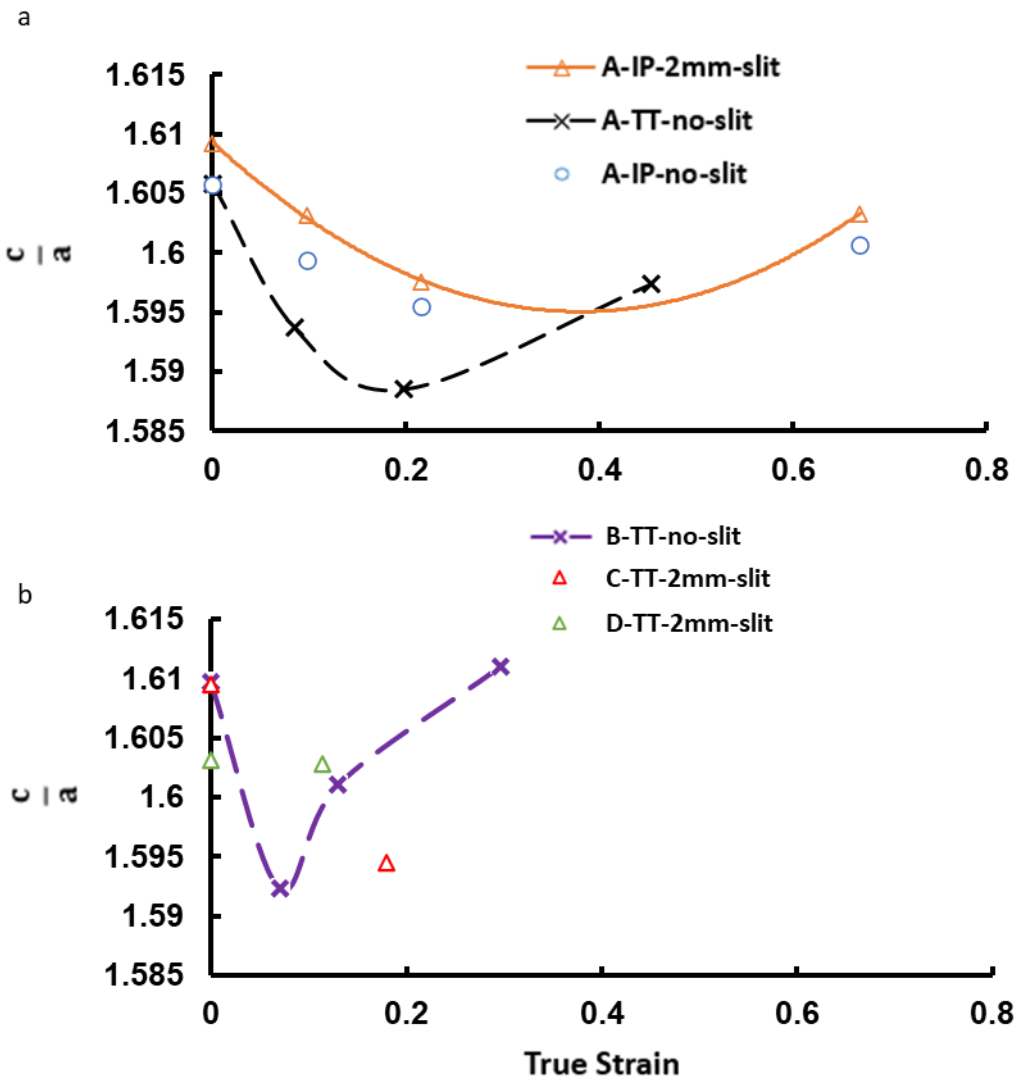

Figure 5: $\frac{c}{a}$ ratio measured by NeD for the samples from the four material categories.

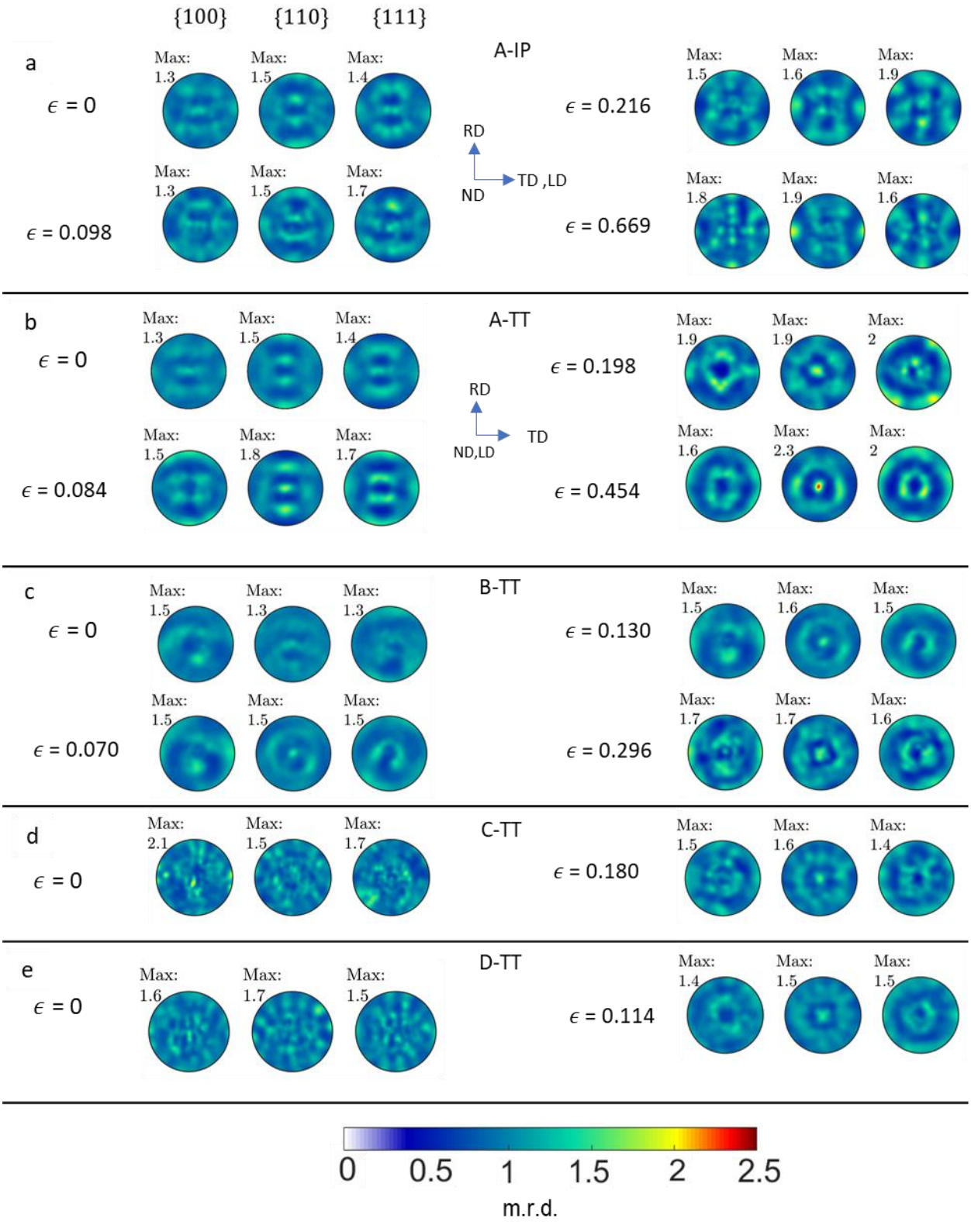
{100}
{110}
{111}
a
ϵ = 0
Max: 1.3
Max: 1.5
Max: 1.4
ϵ = 0.098
Max: 1.3
Max: 1.5
Max: 1.7
A-IP
RD
TD ,LD
ND
ϵ = 0.216
Max: 1.5
Max: 1.6
Max: 1.9
ϵ = 0.669
Max: 1.8
Max: 1.9
Max: 1.6
b
ϵ = 0
Max: 1.3
Max: 1.5
Max: 1.4
ϵ = 0.084
Max: 1.5
Max: 1.8
Max: 1.7
A-TT
RD
TD
ND,LD
ϵ = 0.198
Max: 1.9
Max: 1.9
Max: 2
ϵ = 0.454
Max: 1.6
Max: 2.3
Max: 2
c
ϵ = 0
Max: 1.5
Max: 1.3
Max: 1.3
ϵ = 0.070
Max: 1.5
Max: 1.5
Max: 1.5
B-TT
ϵ = 0.130
Max: 1.5
Max: 1.6
Max: 1.5
ϵ = 0.296
Max: 1.7
Max: 1.7
Max: 1.6
d
ϵ = 0
Max: 2.1
Max: 1.5
Max: 1.7
C-TT
ϵ = 0.180
Max: 1.5
Max: 1.6
Max: 1.4
e
ϵ = 0
Max: 1.6
Max: 1.7
Max: 1.5
D-TT
ϵ = 0.114
Max: 1.4
Max: 1.5
Max: 1.5
0
0.5
1
1.5
2
2.5
m.r.d.

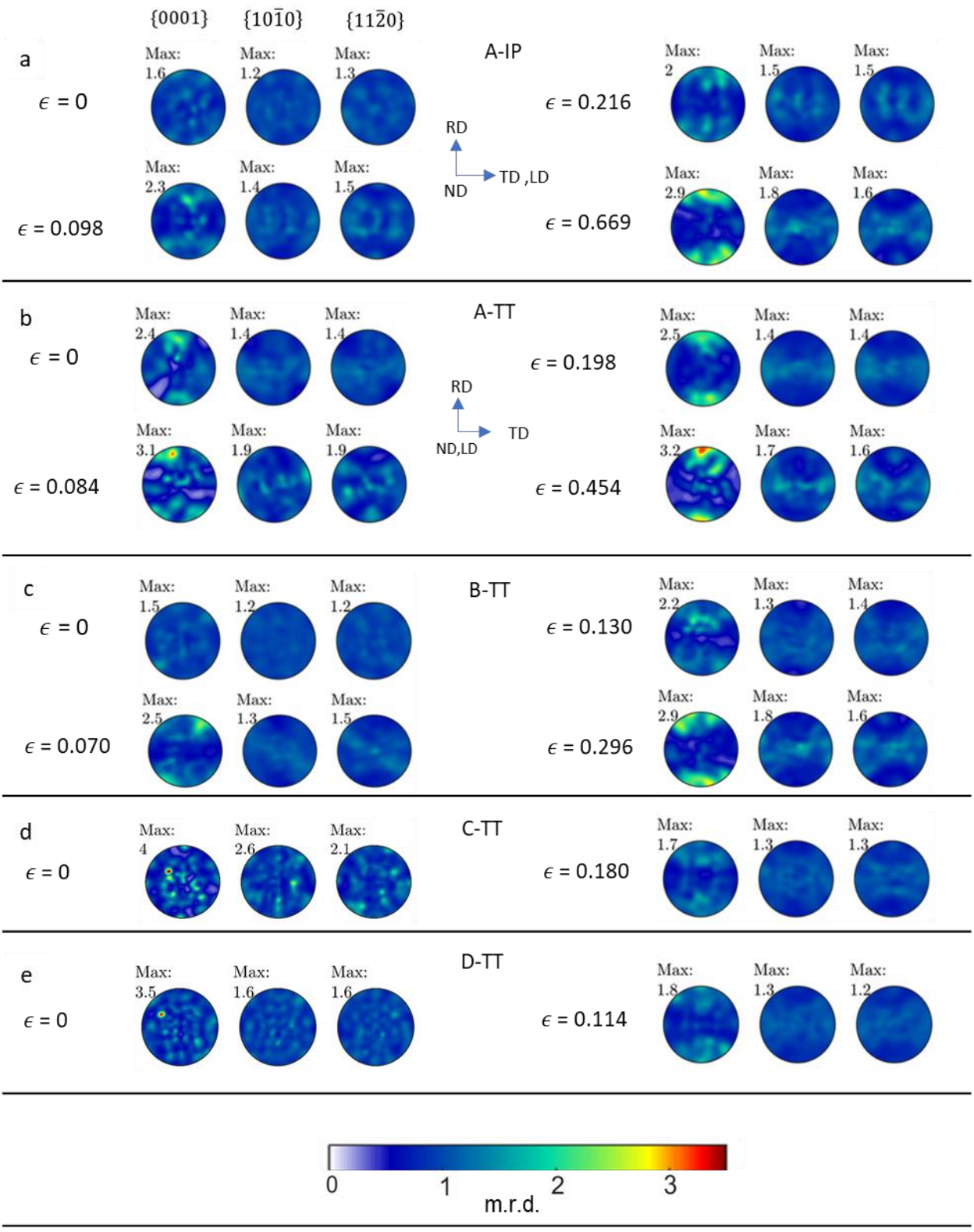
{0001}
{10$\bar{1}$0}
{11$\bar{2}$0}
a
ϵ = 0
Max: 1.6
Max: 1.2
Max: 1.3
A-IP
ϵ = 0.216
Max: 2
Max: 1.5
Max: 1.5
RD
TD ,LD
ND
ϵ = 0.098
Max: 2.3
Max: 1.4
Max: 1.5
ϵ = 0.669
Max: 2.9
Max: 1.8
Max: 1.6
b
ϵ = 0
Max: 2.4
Max: 1.4
Max: 1.4
A-TT
ϵ = 0.198
Max: 2.5
Max: 1.4
Max: 1.4
RD
TD
ND,LD
ϵ = 0.084
Max: 3.1
Max: 1.9
Max: 1.9
ϵ = 0.454
Max: 3.2
Max: 1.7
Max: 1.6
c
ϵ = 0
Max: 1.5
Max: 1.2
Max: 1.2
B-TT
ϵ = 0.130
Max: 2.2
Max: 1.3
Max: 1.4
ϵ = 0.070
Max: 2.5
Max: 1.3
Max: 1.5
ϵ = 0.296
Max: 2.9
Max: 1.8
Max: 1.6
d
ϵ = 0
Max: 4
Max: 2.6
Max: 2.1
C-TT
ϵ = 0.180
Max: 1.7
Max: 1.3
Max: 1.3
e
ϵ = 0
Max: 3.5
Max: 1.6
Max: 1.6
D-TT
ϵ = 0.114
Max: 1.8
Max: 1.3
Max: 1.2
0
1
2
3
m.r.d.

Figure 6: Stereographic pole figures showing the evolution of texture in austenite and martensite phases during compression at the indicated strain levels for: (a) A-IP, (b) A-TT, (c) B-TT, (d) C-TT, and (e) D-TT sample categories. For A-IP, the data from 2 mm slit is presented.

4 Discussion

In order to rationalize the evolution of strength of the HEA studied in this work, it is important to reflect on the thermodynamics of microstructure and phase evolution in the material. The metastable phase of austenite, γ, has an activation barrier for the diffusionless (no partitioning of elements) transformation to a stable phase ε at a given temperature and composition. The ε phase is stable in the Fe-Mn-Co-Cr HEA system at room temperature. The change in Gibb's free energy or the driving force for $\gamma \rightarrow \varepsilon$ transformation ($\Delta G^{\gamma \rightarrow \varepsilon}$ in J/mol) is related to the change in entropy ($\Delta S_{config}^{\gamma \rightarrow \varepsilon}$) using $\Delta G^{\gamma \rightarrow \varepsilon} = \Delta H_{mix}^{\gamma \rightarrow \varepsilon} - T\Delta S_{config}^{\gamma \rightarrow \varepsilon}$ [31]. Here, the $\Delta H_{mix}^{\gamma \rightarrow \varepsilon}$ is the enthalpy of mixing effect on the transformation kinetics and T is the temperature in K. The metastability of γ for $\gamma \rightarrow \varepsilon$ transformation is increased by adding the ε phase stabilizers, Co and Si, which increase $\Delta S_{config}^{\gamma \rightarrow \varepsilon}$ and is in the core of high entropy approach. These not only increase $\Delta S_{config}^{\gamma \rightarrow \varepsilon}$ to increase the metastability of γ for easy $\gamma \rightarrow \varepsilon$ transformation but also lower the SFE of the material. As already mentioned, if SFE is sufficiently low, formation of ε-martensite is favored. Microstructural defects introduced by plasticity such as slip bands are necessary for strain-induced transformation [42, 43]. Under the action of a local stress field separation between partials increases to form a slip band. Such bands usually include multiple dislocations on nearby $\{111\}_\gamma$ planes. These partial dislocations on neighboring $\{111\}_\gamma$ planes are boundaries of a thick fault [44]. If dislocations are positioned at every 2nd $\{111\}_\gamma$ plane in a slip band in γ, the band has HCP structure, which is ε. In contrast, if dislocations are positioned at every $\{111\}_\gamma$ plane in a slip band in γ, the band has FCC structure, which is a twin. Whether ε or twin formation within a slip band is favored depends on the SFE. A higher value of SFE favors formation of twins. The intrinsic SFE (γ_{SFE}) is directly related to $\Delta G^{\gamma \rightarrow \varepsilon}$ using $\gamma_{SFE} = n\rho\Delta G^{\gamma \rightarrow \varepsilon} + n\sigma^{\gamma/\varepsilon}$ [31], where, $\sigma^{\gamma/\varepsilon}$ is the interfacial energy between γ and ε phases, ρ is the planar density of closed packed $\{111\}$ planes, and n is the thickness of an HCP embryo. The interfacial energy barrier for ε phase formation is low because of coherency.

Lowering the γ_{SFE}, the stress required for the dissociation of perfect dislocations into partials in the γ matrix to form stable intrinsic stacking faults also decreases.

However, keeping the composition, i.e. $\Delta S_{config}^{\gamma\rightarrow\varepsilon}$ constant, $\Delta G^{\gamma\rightarrow\varepsilon}$ can be changed using material's stored energy (accumulated strain level), which is embedded in the $\Delta H_{mix}^{\gamma\rightarrow\varepsilon}$ term. Therefore, the enthalpy term varies with prior processing [45]. The last effect to $\Delta G^{\gamma\rightarrow\varepsilon}$ comes from the temperature. In our work, the FSP conditions govern these strain and temperature effects on the transformation kinetics [31]. In summary, accommodated strain and temperature increase are competing effects promoting ε and γ, respectively. The added effects come from size and geometry of grains and dislocation structures. Given the two tool rotation rates explored in the present work, we define two scenarios. In the *scenario 1*, the tool rotation rate is 350 RPM and a higher temperature develops. The FSP substantially refines grains with some recovery, dynamic recrystallization, and grain growth takin place [22]. In the *scenario 2*, the tool rotation rate is 150 RPM and a higher stored energy accumulates in the material because of the lower temperature than at 350 RPM. Note that both tool rotation rates take the material into the γ phase to sufficiently soften the material for FSP. While the plastic deformation is enhanced with higher FSP rotational speed, the 350 RPM rate induces a higher temperature (~900^0C) than the 150 RPM FSP (~700^0C) promoting the softening effects of the material at the high temperature. As a result of lower temperature in FSP at 150 RPM, the material is less recovered and accumulates higher dislocation density and underlying stored energy, which in turn reduces the barrier to $\gamma\rightarrow\varepsilon$ transformation. The high stored energy state of the material corresponds to the high enthalpy state. We emphasize that different processing conditions leave γ in different states of enthalpy, while the entropy remains same as the solid solution configuration remains the same. As a result, the ε phase is thermodynamically more present and stable at room temperature upon FSP at 150 RPM than upon FSP at 350 RPM. In summary, as the strain rate, strain, and temperature depending on the tool rate at which the material is processed change, stored dislocation density changes in the microstructure at high temperature. This initial high temperature structure influences microstructure formation during cooling from γ to room temperature ($\gamma + \varepsilon + \sigma$).

The phases are determined by NeD and EBSD and also verified by optical microscopy (see appendix) in the materials before performing compression and during compression. Consistent

with the above discussion, the fraction of phases is evidently a strong function of processing history. The as-rolled material (A) microstructure contains a small amount of ε phase fraction (~0.12), a higher amount of σ-phase fraction (~0.21), and the highest amount of γ phase fraction (~0.66). The material exhibits a great deal of true strain before fracture with more in the IP than in the TT direction. While the phase fractions at fracture appear similar, the transformation rates are different. The $\gamma \rightarrow \varepsilon$ transformation rate in the TT is greater than in the IP during compression. We attribute this difference in the transformation rate as a function of compression direction to texture.

The strain-induced transformation is strongly affected by texture, i.e. by individual crystal orientation of grains undergoing the transformation [46-51]. In general, soft grains have a higher tendency to transform. In tension, grains with <011> and <111> parallel to a tensile direction form slip bands of ε, while grains with <001> parallel to tensile direction do not produce slip bands [47] because partial dislocations do not have sufficient driving force to produce wide stacking faults [50]. The effect of crystal orientation on the transformation kinetics in compression is reversed. Crystals with the <001> orientation parallel to a compression direction easily transform [49], the crystals compressed along <011> or <011> cannot transform under compression [47]. Inverse pole figures (IPFs) showing the local crystal orientations in the samples relative to the compression direction are provided in the appendix for easier recognition of the texture effects on the transformation in addition to the pole figures. Comparing the IPFs of the A category samples deformed in the IP direction versus in the TT direction reveals a higher number of crystals with the <001> direction parallel to the compression direction in the TT sample. These texture effects on the rate of transformation likely play a role for compressive strain at fracture. The IP samples deforming at a lower transformation rate accumulate more strain before fracture.

To better observe the strain induced phase transformation, a high resolution EBSD map is provided in Fig. 7 for an A sample at a compressive strain of $\epsilon = 0.198$. This meso-scale data is used to verify the macroscopic NeD measurements and evaluate occurrence of any deformation twinning in the structure. Slip bands of the γ as sheaves of fine parallel laths strung out on the $\{111\}_{\gamma}$ planes of the γ phase carry out the strain-induced ε martensite formation while accommodating plastic strain. The ε-martensite phase was not observed to further transform to α'-martensite. The fraction of the diffusion created σ phase during processing does not change during compression at room temperature meaning that the σ phase can only stably form in DP-5Si-HEA

during cooling from high temperature and not because of mechanical straining. The Kernel average misorientation (KAM) map shows a higher presence of geometrically necessary dislocations (GNDs) in the highly dislocated ε phase upon TRIP than in the γ phase. The ε phase is thus harder contributing to the overall hardening of the material, in addition to the dynamic Hall-Petch-type hardening as a consequence of more interfaces in the microstructure forming barriers to mobile dislocations. Therefore, the material exhibits a great deal of strain hardening during compression.

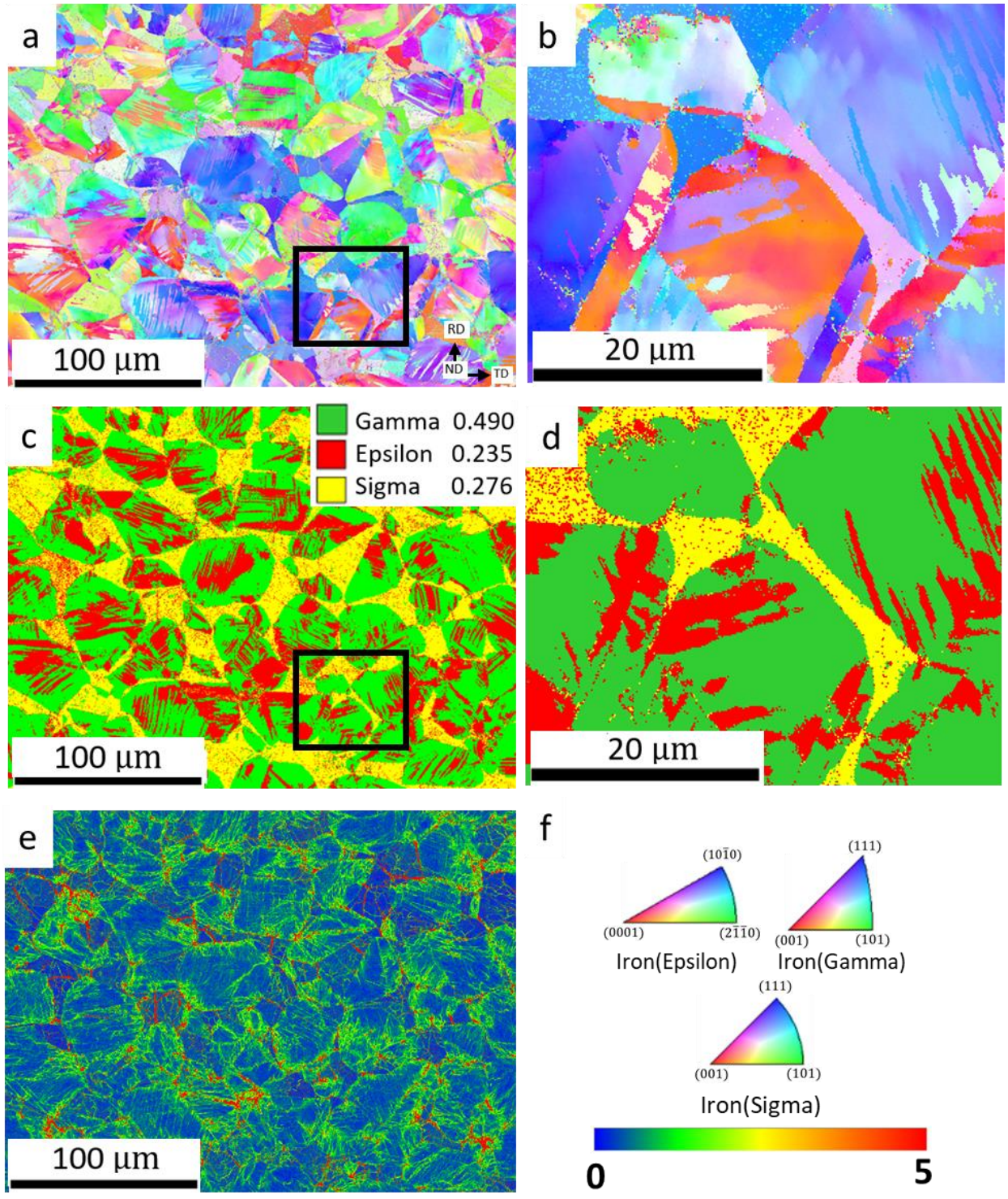

Figure 6: (a, b) IPF, (c, d) phase, and (e) KAM maps obtained by EBSD for the A-TT-0.198 sample. (b, d) are zoom ins. Perpendicular to the IPF map is the ND, which is also the compression

loading direction. (f) ND standard IPF triangles for Iron (γ), Iron (ε) and Iron (σ) phases and the intensity bar for the KAM map.

FSP of the as-rolled material increases the strength, which is attributed to the microstructural changes as described above. The B category samples underwent FSP at 350 RPM, the processing condition of higher strain rate and temperature, and a faster cooling rate after the processing relative to FSP at 150 RPM. Because the temperature has dominated over the strain at 350 RPM (the scenario 1), the fraction of γ even increased (~0.81) at the expanse of ε (0.067) and σ (0.12) relative to the initial A category material. However, the average grain size substantially decreased to 4 μm after the processing. As a result of fine grain size, the B material is stronger than the A material even though it has less of harder ε and σ phases. The low fraction of the σ phase is due to the fast cooling rate preventing the diffusion driven precipitation of the phase in the microstructure [32]. The low fraction of the ε phase is due to the high temperature conditions governing a low dislocation density driven stored energy. Moreover, the material B exhibits even more rapid hardening than the material A, which is attributed to a greater transformation rate from a very large fraction of γ phase. Although the higher rate of transformation is associated primarily to the initially large fraction of deforming γ, grain size may play a secondary role. As grain boundaries act as nucleation sites for ε, back-stress fields and higher stability of grain boundaries hinders the growth of ε [18, 52, 53]. We observe that ε phase starts from grain boundaries at the provided maps in the appendix for B-TT-0.296 sample. No deformation twins are observed in this map as well. The IPF from the appendix shows that γ phase crystal orientations have sufficient preferential orientation for transformation, although the intensity of them is lower than the A category. The rate of TRIP is likely higher in the IP than in the TT sample.

In contrast to A and B material categories, the C material category created by FSP at 150 RPM contains a much larger fraction of harder ε and σ phases (~0.42). The large fraction of ε in the microstructure before compression is a consequence of high stored energy induced during FSP (the scenario 2). The higher σ-phase in C compared to the B category specimens could be because of the operation of FSP at ~700^0C which is known to be the favorable σ-phase precipitation region [32]. The grain size is refined (2 μm) relative to the as-rolled material, A. Owing to the grain structure and phase content, the material is strong and still accumulates a decent amount of TRIP accommodated compressive strain and hardening. Peak broadening and micro-strain increase with

plastic strain of the ε phase suggests that the phase is deforming, which contributes to the plasticity of the alloy. The C material category exhibits a lower rate of phase transformation than B, which is attributed to the lower content of γ and some strain accommodation by ε [18]. The IPFs provided in the appendix show some intensity around <001> direction, especially for the IP sample governing some anisotropy in strain hardening with more in IP than in TT.

The D category samples that underwent double pass (two consecutive FSP passes at 350 RPM followed by 150 RPM) are the strongest. The combined phase fraction of ε and σ in these samples is (~0.41), like in the C material category while the ε phase fraction decreased (~0.13). The presence of higher σ phase fraction can be a consequence of finer grain size after 350 RPM FSP than after as-rolled material providing much more nucleation sites at the grain boundary and favorable 700^0C during 150 RPM FSP processing. The average grain size is about 1 μm. As a result of phase fractions and grain size, the material is the strongest and reaches UTS of 1850 MPa. Furthermore, the IPF in the appendix shows some amount of γ favorably oriented for transformation. The TRIP effect has a slightly higher rate in D than the C material category, despite undergoing the same final FSP processing.

The evolution of texture in the γ phase due to compressive strain shows the formation of a typical $\{110\}$ fiber. After analyzing the texture components, it was observed that the brass, copper and Goss components predominate. On the other hand, the texture formation of the ε phase is primarily driven by the variant selection of the TRIP mechanism. The orientation relationship between γ and ε is $\{111\}_\gamma \parallel \{0001\}_\varepsilon$, $\langle 110\rangle_\gamma \parallel \langle 2\bar{1}\bar{1}0\rangle_\varepsilon$ [54]. While ε phase is stronger than the γ phase, the strength differential is not such to prevent dislocation slip in the ε phase. Therefore, the phases are co-deforming and a minor contribution to texture evolution in the ε phase is due to slip in it. While twins are not observed by EBSD, existence of nano-twins in ε is not ruled out. However, existence of nano-twins would not appreciably influence the texture evolution but would influence strain hardening by restricting the slip length associated with slip. Finally, the texture analysis of the σ phase reveals a random texture throughout the compression deformation indicating that the phase likely does not deform. The texture may be slightly evolving only by the rigid rotation of the σ precipitations.

The intrinsic $\frac{c}{a}$ ratio in metals like Mg or Be or Ti alloys does not change during deformation. In a dual phase HEA ($Fe_{50}Mn_{30}Co_{10}Cr_{10}$), the $\frac{c}{a}$ ratio of 1.616 is reported in the literature [55]. As expected, changes in alloying change the $\frac{c}{a}$ ratio. The addition of Co, Mn and Si (HCP stabilizers) increases the lattice distortion and the $\frac{c}{a}$ ratio, while the addition of austenite stabilizers such as Cu or Al decreases the $\frac{c}{a}$ ratio. For all the cases, the $\frac{c}{a}$ ratio was lower than the ideal $\frac{c}{a}$ = 1.633. However, processing history of such HEA can change the $\frac{c}{a}$ ratio. For CS-HEA, the ratio decreases from as-cast 1.6254 to FSP 1.615 and further to ~1.598 for samples fractured in tension [56]. The present work observed similar changes in the $\frac{c}{a}$ ratio for $Fe_{42}Mn_{28}Co_{10}Cr_{15}Si_5$ HEA. While the actual origin of lattice parameter changes with plasticity is not known, these changes in $\frac{c}{a}$ for ε-martensite have been attributed to the volume reduction (~1.6%) that occurs during $\gamma \rightarrow \varepsilon$ transformation and underlying shear as well as shuffle along the habit plane for **a**-axis and perpendicular to the plane for **c**-axis [56]. The change in $\frac{c}{a}$ is likely increasing the ductility by shifting relative activity of slip systems since in HCP metals $\frac{c}{a}$ ratio influences the selection of mode of deformation accommodating an applied plastic strain: basal <**a**>, prismatic <**a**>, and pyramidal <**c**+**a**> slip or twinning. HCP metals with lower than the ideal ratio have a higher probability for activating <**c**+**a**> slip systems, which given their multiplicity improve ductility. Given the low $\frac{c}{a}$ ratio of ε, <**c**+**a**> slip operates in the alloy as observed in [18, 56].

In closing, to verify the formation of σ phase, we show a secondary electron (SE) SEM micrograph along with energy-dispersive X-ray spectroscopy (EDS) elemental maps of the same area for an A-TT initial sample in Fig. 8. Given the composition of the alloy, the cooling rates during processing were such that the kinetics of σ diffusion transformation was operating in the 600 ˚ – 1000 ˚C temperature range. The kinetics during cooling in FSP also created the σ-phase but the structure was much finer than upon rolling. As discussed earlier, the σ phase is an intermetallic forming at the Cr rich regions. Figs. 8b and c verify the high Si and Cr at the σ-phase region. Additionally, the spot analysis validates higher Cr and Si at% in the sigma phase (Table 3). Interestingly, some untransformed γ phases is present as colonies of small particles in the σ-phase. A high resolution EBSD map verifying the untransformed γ phase in σ is presented in the appendix.

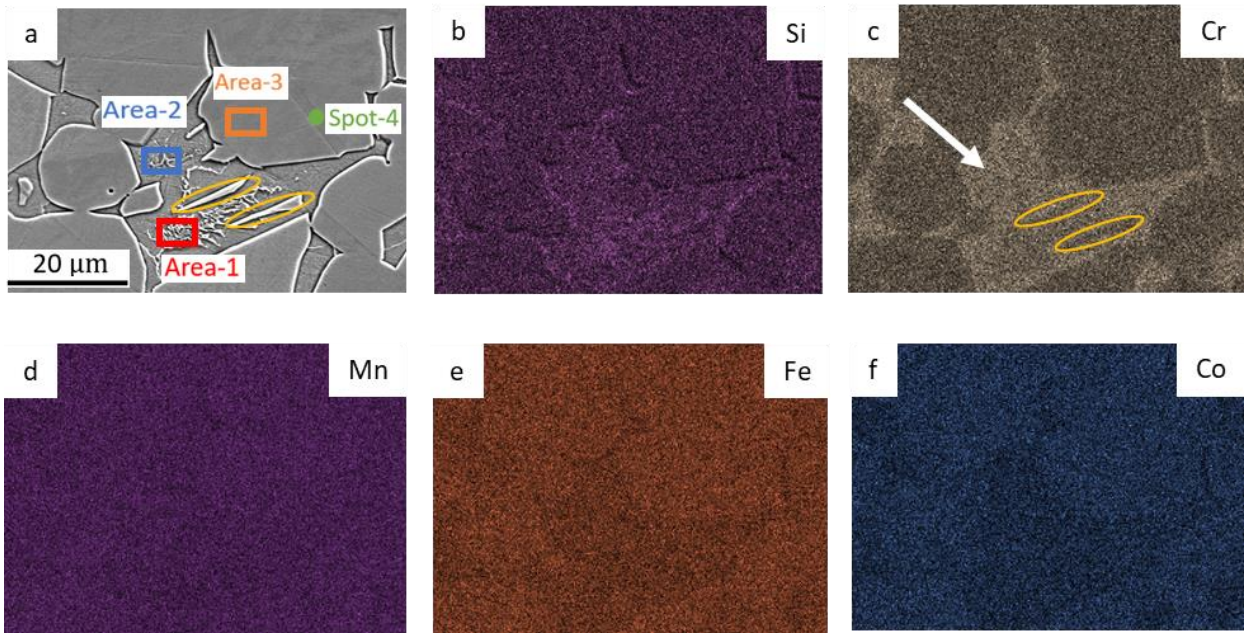

Figure 7: SEM-SE micrograph of A-TT category (a). The composition maps of (b) Si, (c) Cr, (d) Mn, (e) Fe, and (f) Co. The composition map shows a higher Cr in σ-phase (denoted with the white arrow). Yellow ellipses in (a) and (c) show low Cr phases inside a higher Cr zone. These were identified as γ phases using EBSD.

Table 3: EDS measured composition at the marked regions and points in Fig. 8a. EDS over very large area recovers accurately the nominal composition.

	Position	Si (at%)	Cr (at%)	Mn (at%)	Fe (at%)	Co (at%)
A-TT-initial	Area-1	4.97	17.78	27.85	41.72	7.69
	Area-2	3.84	19.80	28.11	40.65	7.60
	Area-3	3.21	14.17	29.95	43.22	9.46
	Spot-4	3.25	14.57	29.89	42.96	9.33
	Nominal	5.00	15.00	28.00	42.00	10.00

5 Conclusions

In this study, strength and microstructure evolution of a very low SFE $Fe_{42}Mn_{28}Co_{10}Cr_{15}Si_5$ (in at%) HEA were investigated. The primarily focus was on the evolution during compression of the initial microstructures created by rolling and FSP. The initial microstructures had triplex structure consisting of metastable γ, stable σ, and stable ε phases in different ratios and various grain sizes depending on the processing. FSP at 350 RPM slightly increased the γ phase content to that created by rolling but substantially refined grains. In contrast, the FSP at 150 RPM increased the fraction of ε phase along with refining the grain structure. Finally, the FSP with 350 RPM followed by 150 RPM significantly refined the structure and also increased fraction of the σ phase. The tremendous microstructural flexibility exhibited by the alloy facilitates a creation of the material with 1850 MPa UTS. In the core of the flexibility is the transformation facilitated plastic strain accommodation and underlying strain hardening. The hardening is a consequence of the increased fraction of the highly dislocated ε phase fraction and transformation induced dynamic Hall-Petch-type barrier effect. Strain to fracture of the material is greater with a larger amount of the γ phase and a slower rate of TRIP. The rate of TRIP was found to increase with the initial content on γ and favorable texture i.e. more grains with the <001> orientation parallel to a compression direction. Texture of γ phase exhibits strengthening of $\{110\}$ fiber along the compression direction, while the texture formation of the ε phase is primarily driven by the variant selection of the TRIP mechanism. Given the measured low $\frac{c}{a}$ ratio of ε with a decreasing trend with plastic strain, the activation of non-basal slip systems contributing to the ductility of the alloy is promoted. Therefore, some texture evolution in ε is due to slip as the phases are co-deforming. The texture analysis of the σ phase reveals a random texture throughout the compression deformation, which means that the phase likely does not deform but only floats in the matrix.

While twins were not observed by EBSD, existence of nano-twins in ε is not ruled out. Transmission electron microscopy (TEM) analyses of the alloy is needed to observe any presence of nano-twins in the ε phase. These twins are important as they could influence the strain hardening rates in the alloy by restricting the slip length associated with slip.

Acknowledgements

This research was sponsored by the U.S. Army Research Laboratory under the W911NF-15-2-0084 cooperative agreement and the U.S. National Science Foundation under the OIA-1757371 grant.

Appendix

This appendix presents optical microscopy images corresponding to Fig. 3 in Fig. A1, inverse pole figures (IPFs) showing the initial texture in the samples in Fig. A2, deformed structure of B-TT sample at 0.296 strain in Fig. A3, zoom in SEM secondary electrons (SE) image of A-TT-initial sample revealing phases in Fig. A4. Table A1 shows a comparison of measured phase fractions data using three different methods.

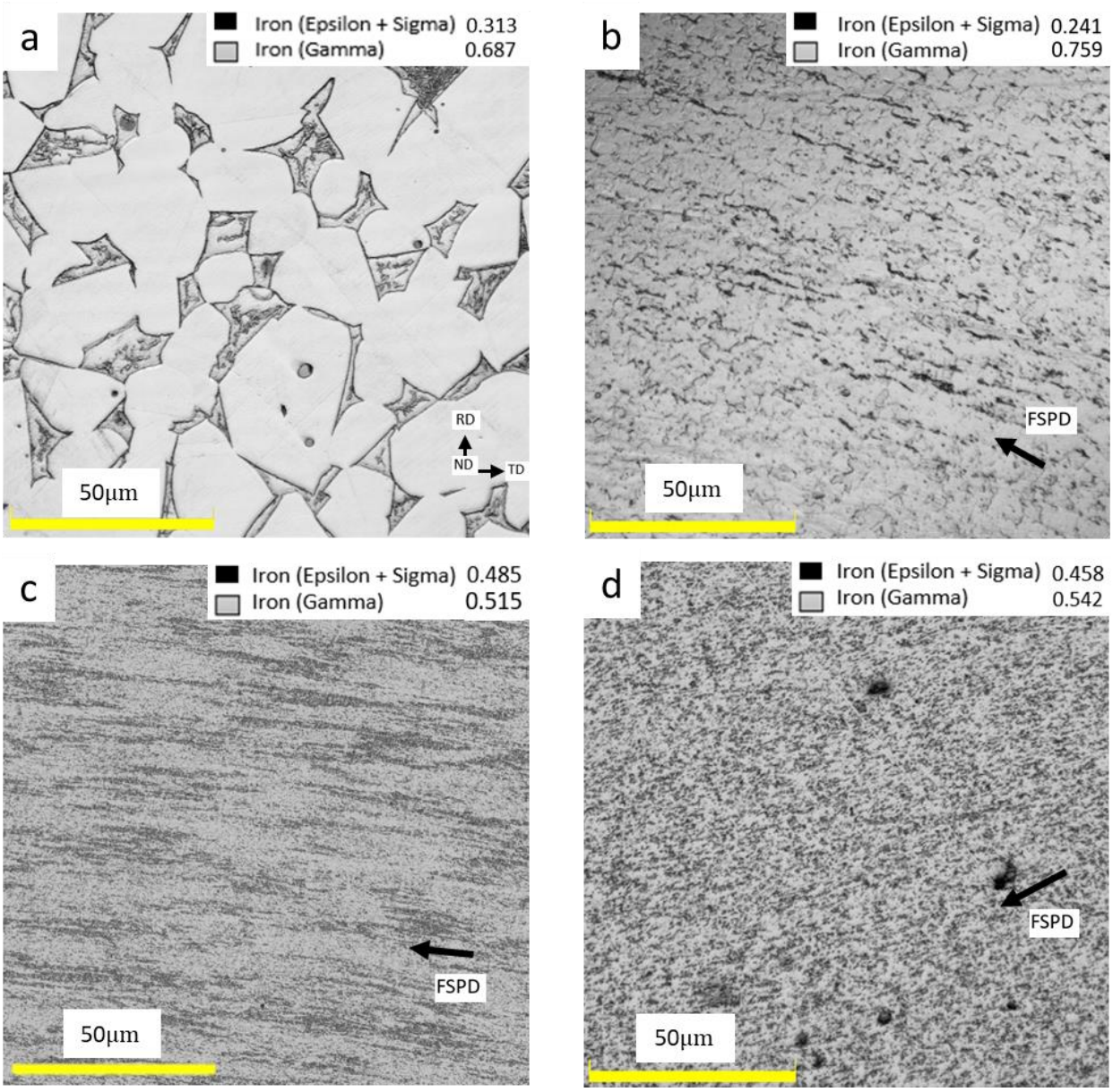

Figure A1: Optical microscopy images for the following samples: (a) A-TT-initial (as rolled), (b) B-TT-initial (FSP at a tool speed of 350 rpm), (c) C-TT-initial (FSP at a tool speed of 150 rpm), and (d) D-TT-initial (FSP with two consecutive runs at tool speeds of 350 RPM and 150 RPM, respectively). Image thresholding in MATLAB is used to obtain the phase fractions. The reported fraction values are averaged over at least 3 images per sample category. The white regions are gamma phase, while the black areas are epsilon and sigma phases.

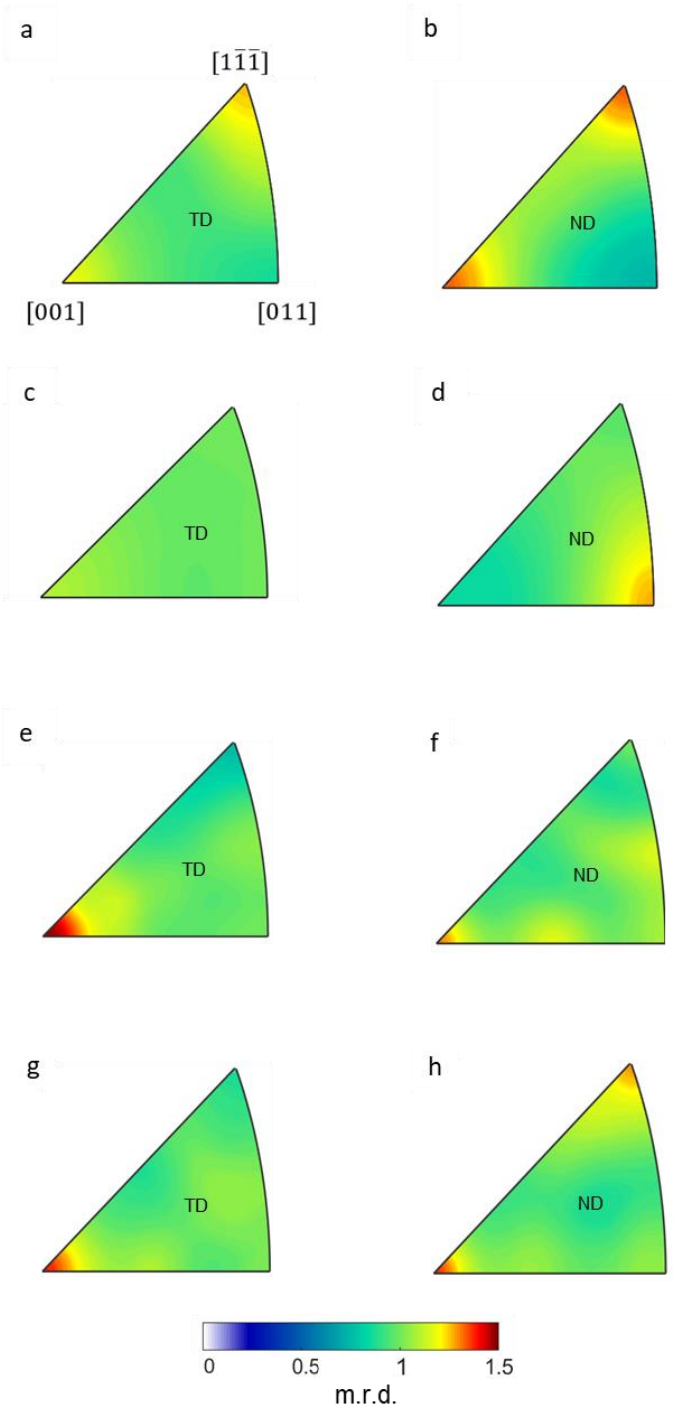

Figure A2: Inverse pole figures (IPFs) showing texture relative to the loading direction in: (a) A-IP, (b) A-TT, (c) B-IP, (d) B-TT, (e) C-IP (f) C-TT, (g) D-IP, and (h) D-TT samples.

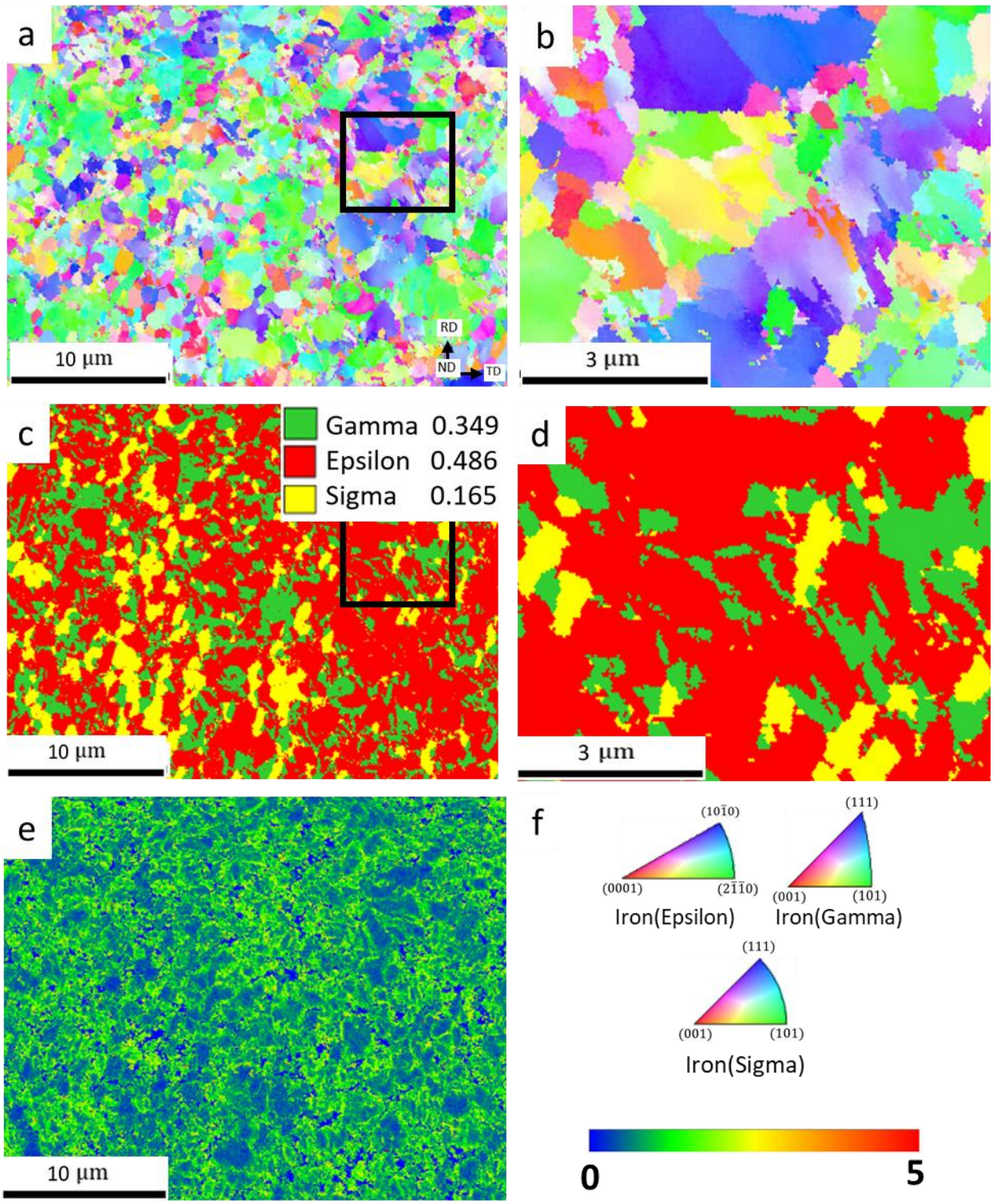

Figure A3: (a,b) IPF, (c,d) phase, and (e) KAM maps obtained by EBSD for a B-TT-0.296 sample. (b,d) are zoom ins. Although the red and yellow color represent the epsilon and sigma phase respectively (c,d), their fraction was not reported because of the low confidence index. Perpendicular to the maps is the sample ND, which is also the compression direction. (f) ND

standard IPF triangles for Iron (γ), Iron (ε) and Iron (σ) phases and the intensity bar for the KAM map.

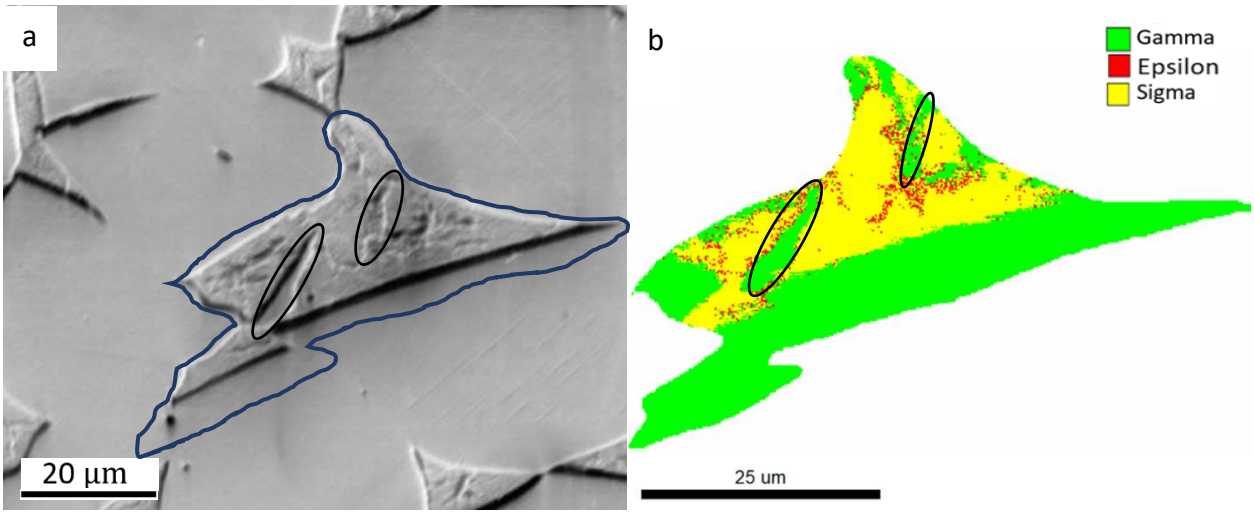

Figure A4: (a) SEM–SE micrograph for A-TT-initial sample at 70^0 tilt. (b) The corresponding EBSD phase map for the selected area surrounded by the blue color. The black ellipses show γ phase inside σ phase.

Table A1: Measured phase fractions data using three different methods.

	NeD			Optical images thresholding		EBSD		
	Gamma	Epsilon	Sigma	Gamma	Epsilon + Sigma	Gamma	Epsilon	Sigma
D-TT-initial-0.0	0.583	0.131	0.286	0.542	0.458	0.571	0.122	0.307
C-TT-initial-0.0	0.579	0.224	0.197	0.515	0.485	0.542	0.229	0.229
B-TT-initial-0.0	0.814	0.067	0.118	0.759	0.241	0.723	0.138	0.139
B-TT-0.070	0.660	0.221	0.118	-----	-----	-----		

B-TT-0.130	0.610	0.271	0.118	-----	-----	-----		
B-TT-frac-0.296	0.482	0.384	0.118	0.366	0.636	0.349	0.486	0.165
D-TT-frac-0.114	0.487	0.227	0.286	0.484	0.516	-----		
C-TT-frac-0.18	0.469	0.331	0.229	0.495	0.505	-----		
A-TT-initial-0.0 (A-IP-initial-no-slit)	0.663	0.119	0.218	0.687	0.313	0.653	0.139	0.208
A-TT-0.085	0.634	0.148	0.218	------	------	------		
A-TT-0.198	0.522	0.260	0.218	------	------	0.49	0.235	0.275
A-TT-frac-0.454	0.306	0.476	0.218	0.315	0.685	------		
A-IP-0.098 (no slit)	0.528	0.254	0.218	------	------	------		
A-IP-0.215 (no slit)	0.476	0.306	0.218	------	------	------		
A-IP-frac-0.669 (no slit)	0.333	0.449	0.218	------	------	------		
A-IP-initial-0.0 (2mm slit)	0.670	0.119	0.211	------	------	------		
A-IP-0.098 (2mm slit)	0.575	0.214	0.211	------	------	------		

A-IP-0.215 (2mm slit)	0.510	0.278	0.211	------	------	------
A-IP-frac-0.669 (2mm slit)	0.325	0.464	0.211	------	------	------

References

[1] B. Cantor. Multicomponent and high entropy alloys, Entropy 16 (2014) 4749-4768.

[2] J.W. Yeh, S.K. Chen, S.J. Lin, J.Y. Gan, T.S. Chin, T.T. Shun, C.H. Tsau, S.Y. Chang. Nanostructured high-entropy alloys with multiple principal elements: novel alloy design concepts and outcomes, Advanced Engineering Materials 6 (2004) 299-303.

[3] Z. Li, K.G. Pradeep, Y. Deng, D. Raabe, C.C. Tasan. Metastable high-entropy dual-phase alloys overcome the strength–ductility trade-off, Nature 534 (2016) 227-230.

[4] Z. Li, C.C. Tasan, K.G. Pradeep, D. Raabe. A TRIP-assisted dual-phase high-entropy alloy: Grain size and phase fraction effects on deformation behavior, Acta. Mater. 131 (2017) 323-335.

[5] Y. Deng, C.C. Tasan, K.G. Pradeep, H. Springer, A. Kostka, D. Raabe. Design of a twinning-induced plasticity high entropy alloy, Acta Materialia 94 (2015) 124-133.

[6] Z. Li, D. Raabe. Strong and ductile non-equiatomic high-entropy alloys: design, processing, microstructure, and mechanical properties, Jom 69 (2017) 2099-2106.

[7] M.J. Yao, K.G. Pradeep, C.C. Tasan, D. Raabe. A novel, single phase, non-equiatomic FeMnNiCoCr high-entropy alloy with exceptional phase stability and tensile ductility, Scripta Materialia 72-73 (2014) 5-8.

[8] B. He, B. Hu, H. Yen, G. Cheng, Z. Wang, H. Luo, M. Huang. High dislocation density–induced large ductility in deformed and partitioned steels, Science 357 (2017) 1029-1032.

[9] S.S. Nene, M. Frank, K. Liu, S. Sinha, R.S. Mishra, B. McWilliams, K.C. Cho. Reversed strength-ductility relationship in microstructurally flexible high entropy alloy, Scr. Mater. 154 (2018) 163-167.

[10] Z. Feng, M. Zecevic, M. Knezevic. Stress-assisted ($\gamma \rightarrow \alpha'$) and strain-induced ($\gamma \rightarrow \varepsilon \rightarrow \alpha'$) phase transformation kinetics laws implemented in a crystal plasticity model for predicting strain path sensitive deformation of austenitic steels, Int. J. Plast. 136 (2021) 102807.

[11] B.C. De Cooman, Y. Estrin, S.K. Kim. Twinning-induced plasticity (TWIP) steels, Acta Materialia 142 (2018) 283-362.

[12] S.S. Nene, K. Liu, M. Frank, R.S. Mishra, R.E. Brennan, K.C. Cho, Z. Li, D. Raabe. Enhanced strength and ductility in a friction stir processing engineered dual phase high entropy alloy, Scientific reports 7 (2017) 1-7.

[13] R. Xiong, H. Peng, S. Wang, H. Si, Y. Wen. Effect of stacking fault energy on work hardening behaviors in Fe–Mn–Si–C high manganese steels by varying silicon and carbon contents, Materials & Design 85 (2015) 707-714.

[14] E. Galindo-Nava, P. Rivera-Díaz-del-Castillo. Understanding martensite and twin formation in austenitic steels: A model describing TRIP and TWIP effects, Acta Materialia 128 (2017) 120-134.
[15] J.J. Jonas, C. Aranas Jr, S.F. Rodrigues. Dynamic transformation of austenite at temperatures above the Ae3. Materials Science Forum, vol. 941: Trans Tech Publ, 2018. p.633-638.
[16] R. Xiong, H. Peng, H. Si, W. Zhang, Y. Wen. Thermodynamic calculation of stacking fault energy of the Fe–Mn–Si–C high manganese steels, Materials Science and Engineering: A 598 (2014) 376-386.
[17] S.S. Nene, M. Frank, K. Liu, R.S. Mishra, B.A. McWilliams, K.C. Cho. Extremely high strength and work hardening ability in a metastable high entropy alloy, Scientific Reports 8 (2018) 9920.
[18] M. Frank, Y. Chen, S.S. Nene, S. Sinha, K. Liu, K. An, R.S. Mishra. Investigating the deformation mechanisms of a highly metastable high entropy alloy using in-situ neutron diffraction, Materials Today Communications 23 (2020) 100858.
[19] A. Heczel, M. Kawasaki, J.L. Lábár, J.-i. Jang, T.G. Langdon, J. Gubicza. Defect structure and hardness in nanocrystalline CoCrFeMnNi high-entropy alloy processed by high-pressure torsion, Journal of Alloys and Compounds 711 (2017) 143-154.
[20] V.H. Hammond, M.A. Atwater, K.A. Darling, H.Q. Nguyen, L.J. Kecskes. Equal-channel angular extrusion of a low-density high-entropy alloy produced by high-energy cryogenic mechanical alloying, Jom 66 (2014) 2021-2029.
[21] N. Kumar, M. Komarasamy, P. Nelaturu, Z. Tang, P. Liaw, R. Mishra. Friction stir processing of a high entropy alloy Al 0.1 CoCrFeNi, Jom 67 (2015) 1007-1013.
[22] S. Palanivel, A. Arora, K. Doherty, R. Mishra. A framework for shear driven dissolution of thermally stable particles during friction stir welding and processing, Materials Science and Engineering: A 678 (2016) 308-314.
[23] R.Z. Valiev, T.G. Langdon. Principles of equal-channel angular pressing as a processing tool for grain refinement, Progress in materials science 51 (2006) 881-981.
[24] A.P. Zhilyaev, T.G. Langdon. Using high-pressure torsion for metal processing: Fundamentals and applications, Progress in Materials science 53 (2008) 893-979.
[25] S. Nene, M. Frank, K. Liu, S. Sinha, R. Mishra, B. McWilliams, K. Cho. Reversed strength-ductility relationship in microstructurally flexible high entropy alloy, Scripta Materialia 154 (2018) 163-167.
[26] P. Agrawal, S. Shukla, S. Gupta, P. Agrawal, R.S. Mishra. Friction stir gradient alloying: A high-throughput method to explore the influence of V in enabling HCP to BCC transformation in a γ-FCC dominated high entropy alloy, Applied Materials Today 21 (2020) 100853.
[27] H.-R. Wenk, L. Lutterotti, S. Vogel. Texture analysis with the new HIPPO TOF diffractometer, Nuclear Instruments and Methods in Physics Research Section A: Accelerators, Spectrometers, Detectors and Associated Equipment 515 (2003) 575-588.
[28] H.-R. Wenk, L. Lutterotti, S. Vogel. Rietveld texture analysis from TOF neutron diffraction data, Powder Diffraction 25 (2010) 283-296.
[29] C.-C. Hsieh, W. Wu. Overview of intermetallic sigma (?) phase precipitation in stainless steels, International Scholarly Research Notices 2012 (2012).
[30] T. Liang, X.Q. Hu, X.H. Kang, D.Z. Li. Effect of the sigma phase on the mechanical properties of a cast duplex stainless steel during the ageing treatment at 850° C. Advanced Materials Research, vol. 684: Trans Tech Publ, 2013. p.325-329.

[31] S. Nene, M. Frank, P. Agrawal, S. Sinha, K. Liu, S. Shukla, R. Mishra, B. McWilliams, K. Cho. Microstructurally flexible high entropy alloys: Linkages between alloy design and deformation behavior, Materials & Design 194 (2020) 108968.
[32] S. Nene, K. Liu, S. Sinha, M. Frank, S. Williams, R. Mishra. Superplasticity in fine grained dual phase high entropy alloy, Materialia 9 (2020) 100521.
[33] N.C. Ferreri, S.C. Vogel, M. Knezevic. Determining volume fractions of γ, γ′, γ ″, δ, and MC-carbide phases in Inconel 718 as a function of its processing history using an advanced neutron diffraction procedure, Materials Science and Engineering: A 781 (2020) 139228.
[34] S. Takajo, S.C. Vogel. Determination of pole figure coverage for texture measurements with neutron time-of-flight diffractometers, Journal of Applied Crystallography 51 (2018) 895-900.
[35] L.-M. Peng, G. Ren, S. Dudarev, M. Whelan. Debye–Waller factors and absorptive scattering factors of elemental crystals, Acta Crystallographica Section A: Foundations of Crystallography 52 (1996) 456-470.
[36] R.E. Smallman, K.H. Westmacott. Stacking faults in face-centred cubic metals and alloys, Philosophical magazine 2 (1957) 669-683.
[37] J. Häglund, A. Fernández Guillermet, G. Grimvall, M. Körling. Theory of bonding in transition-metal carbides and nitrides, Physical Review B 48 (1993) 11685-11691.
[38] L.S. Dubrovinsky, P. Lazor, S.K. Saxena, P. Häggkvist, H.-P. Weber, T. Le Bihan, D. Hausermann. Study of laser heated iron using third generation synchrotron X-ray radiation facility with imaging plate at high pressures, Physics and Chemistry of Minerals 26 (1999) 539.
[39] G. Bergman, D.P. Shoemaker. The determination of the crystal structure of the [sigma] phase in the iron-chromium and iron-molybdenum systems, Acta Crystallographica 7 (1954) 857-865.
[40] X.-L. Wang, Y. Wang, J. Richardson. Experimental error caused by sample displacement in time-of-flight neutron diffractometry, Journal of applied crystallography 35 (2002) 533-537.
[41] I.C. Noyan, J.R. Bunn, M. Tippett, E. Payzant, B. Clausen, D.W. Brown. Experimental determination of precision, resolution, accuracy and trueness of time-of-flight neutron diffraction strain measurements, Journal of Applied Crystallography 53 (2020) 494-511.
[42] G.B. Olson, M. Cohen. A mechanism for the strain-induced nucleation of martensitic transformations, Journal of the Less Common Metals 28 (1972) 107-118.
[43] G.B. Olson, M. Cohen. Kinetics of strain-induced martensitic nucleation, Metallurgical Transactions A 6 (1975) 791.
[44] G.B. Olson, M. Cohen. A general mechanism of martensitic nucleation: Part I. General concepts and the FCC→ HCP transformation, MTA 7 (1976) 1897-1904.
[45] R.S. Mishra, R.S. Haridas, P. Agrawal. High entropy alloys – Tunability of deformation mechanisms through integration of compositional and microstructural domains, Mater. Sci. Eng. A 812 (2021) 141085.
[46] W.G. Burgers, J.A. Klostermann. Influence of the direction of deformation on the transition of austenite into martensite, Acta Metallurgica 13 (1965) 568-572.
[47] D. Goodchild, W.T. Roberts, D.V. Wilson. Plastic deformation and phase transformation in textured austenitic stainless steel, Acta Metallurgica 18 (1970) 1137-1145.
[48] B. Petit, N. Gey, M. Cherkaoui, B. Bolle, M. Humbert. Deformation behavior and microstructure/texture evolution of an annealed 304 AISI stainless steel sheet. Experimental and micromechanical modeling, International Journal of Plasticity 23 (2007) 323-341.

[49] E. Polatidis, W.N. Hsu, M. Šmíd, T. Panzner, S. Chakrabarty, P. Pant, H. Van Swygenhoven. Suppressed martensitic transformation under biaxial loading in low stacking fault energy metastable austenitic steels, Scr. Mater. 147 (2018) 27-32.
[50] M. Zecevic, M.V. Upadhyay, E. Polatidis, T. Panzner, H. Van Swygenhoven, M. Knezevic. A crystallographic extension to the Olson-Cohen model for predicting strain path dependence of martensitic transformation, Acta. Mater. 166 (2019) 386-401.
[51] R. Lagneborgj. The martensite transformation in 18% Cr-8% Ni steels, Acta Metall. 12 (1964) 823-843.
[52] M. Wang, Z. Li, D. Raabe. In-situ SEM observation of phase transformation and twinning mechanisms in an interstitial high-entropy alloy, Acta Materialia 147 (2018) 236-246.
[53] R.S. Mishra, S.S. Nene, M. Frank, S. Sinha, K. Liu, S. Shukla. Metastability driven hierarchical microstructural engineering: Overview of mechanical properties of metastable complex concentrated alloys, Journal of Alloys and Compounds 842 (2020) 155625.
[54] L. Bracke, L. Kestens, J. Penning. Transformation mechanism of α′-martensite in an austenitic Fe–Mn–C–N alloy, Scripta Materialia 57 (2007) 385-388.
[55] Y. Bu, Z. Li, J. Liu, H. Wang, D. Raabe, W. Yang. Nonbasal Slip Systems Enable a Strong and Ductile Hexagonal-Close-Packed High-Entropy Phase, Physical Review Letters 122 (2019) 075502.
[56] S. Sinha, S.S. Nene, M. Frank, K. Liu, P. Agrawal, R.S. Mishra. On the evolving nature of c/a ratio in a hexagonal close-packed epsilon martensite phase in transformative high entropy alloys, Scientific Reports 9 (2019) 13185.